Multiscale elasticity mapping of biological samples in 3D at optical resolution

Kathryn Regan[1], Robert LeBourdais[1], Rohin Banerji[1], Sue Zhang[1], Johnathan Muhvich[1], Siyi Zheng[1], Hadi T. Nia[1,*]

[1]Department of Biomedical Engineering, Boston University, 44 Cummington Mall, Boston, MA, USA 02215
[*]Corresponding author: Hadi T. Nia Ph.D., htnia@bu.edu

Abstract

The mechanical properties of biological tissues have emerged as an integral determinant of tissue function in health and disease. Nonetheless, characterizing the elasticity of biological samples in 3D and at high resolution remains challenging. Here, we present a μElastography platform: a scalable elastography system that maps the elastic properties of tissues from cellular to organ scales. The platform leverages the use of a biocompatible, thermo-responsive hydrogel to deliver compressive stress to a biological sample and track its resulting deformation. By surrounding the specimen with a reference hydrogel of known Young's modulus, we are able to map the absolute values of elastic properties in biological samples. We validate the experimental and computational components of the platform using a hydrogel phantom and verify the system's ability to detect internal mechanical heterogeneities. We then apply the platform to map the elasticity of multicellular spheroids and the murine lymph node. With these applications, we demonstrate the platform's ability to map tissue elasticity at internal planes of interest, as well as capture mechanical heterogeneities neglected by most macroscale characterization techniques. The μElastography platform, designed to be implementable in any biology lab with access to 3D microscopy (e.g., confocal, multiphoton, or optical coherence microscopy), will provide the capability to characterize the mechanical properties of biological samples to labs across the large community of biological sciences by eliminating the need of specialized instruments such as atomic force microscopy.

Keywords: elastography, mechanobiology, stiffness measurement, biological stiffness, thermo-responsive

Statement of Significance

Understanding the elasticity of biological tissues is of great importance, but characterizing these properties typically requires highly specialized equipment. Utilizing stimulus-responsive hydrogels, we present a scalable, hydrogel-based elastography method that uses readily available reagents and imaging modalities to generate resolved maps of internal elasticity within biomaterials and biological samples at optical resolution. This new approach is capable of detecting internal stiffness heterogeneities within the 3D bulk of samples and is highly scalable across both imaging modalities and biological length scales. Thus, it will have significant impact on the measurement capabilities of labs studying engineered biomaterials, mechanobiology, disease progression, and tissue engineering and development.

1. Introduction

The mechanical properties of biological tissues play a critical role in healthy and diseased processes. Normal mechanical environments are necessary for healthy tissue development [1] and function [2], whereas abnormal mechanical environments have been linked to disease progression: increased stiffness is a major physical hallmark of cancer [3] and is also essential in estimating solid mechanical stresses [4-8], another key physical hallmark of cancer. These alterations in mechanical properties of the tumor

microenvironment influence processes leading to cell proliferation [9], angiogenesis [10], and cell migration [11]. Additionally, alterations to stiffness are also a key physical hallmark within the healthy tissues immediately adjacent to tumors (i.e., peritumor microenvironment), with valuable implications on tumor immunity and immune response [12]. Mechanical abnormalities have also emerged to hold diagnostic [13] and prognostic [14] potential in cancer and fibrotic diseases, and have recently been used as markers for treatment prediction [15, 16] and disease progression [17]. Characterizing the magnitude and distribution of tissue elasticity therefore offers valuable insight into the cause-effect relationship between the mechanical microenvironment and biological activities.

Given this importance, a variety of techniques exist to quantify mechanical properties of biological tissues and engineered biomaterials (Table 1). At the microscale, atomic force microscopy (AFM) has been used as a gold standard for mapping elasticity at high resolution [18, 19], yet this technique typically requires cell monolayers or thin tissue sectioning, which may cause cutting artifacts, and can only generate 2D maps of elasticity at the sample surface. Other microscale methods exist to quantify viscoelastic properties, including particle tracking microrheology [20] and optical tweezers microrheology [21, 22], but these methods are limited to measuring only local properties. Optical coherence elastography methods measure mechanical response at the sub-millimeter scale between cells and organs [23], yet most of these applications either rely on 2D perturbations and therefore result in only 1D or 2D relative measurements, or are difficult to reconstruct into quantitative maps. Brillouin microscopy [24, 25] obtains 3D hydromechanical maps at subcellular resolution, but generates modulus values in the order of GPa for samples with Young's modulus in the order of kPa.

A number of innovative techniques have recently emerged to study mechanical heterogeneities and distributions within biological samples, including microtweezer-induced strain mapping [26, 27], light-sheet optical coherence elastography [28], laser speckle rheology [29], and deformable oil droplets [30]. Some of these emergent techniques, such as thermo-responsive sensors [31], enable highly detailed local measurements over time, yet for the most part these techniques face the same challenges as their predecessors: namely scalability, quantitative nature, and full 3D mapping. Furthermore, the majority of these existing elastography techniques require highly specialized and/or costly equipment that is not readily accessible to many academic and research labs. Thus, a scalable modality that captures internal elasticity maps at a high spatial resolution with absolute (i.e. Pascal) values, while simultaneously preserving the 3D quality of biological tissue, remains elusive.

In this work, we present a new experimental and computational platform to provide elasticity maps of biological tissues at high resolution. Our platform involves delivering a highly controlled, multi-directional compressive stress via a thermo-responsive hydrogel. We then couple a deformable image registration algorithm [32, 33] with finite-element based inverse-problem solving [34, 35] to quantify the resulting deformations at optical resolution (submicron to millimeter depending on the imaging modality) and deliver highly detailed spatial maps of sample elasticity on a user-specified plane of interest. The platform, termed μElastography due to the optical resolution nature of these measurements, is highly scalable and compatible with multiple imaging modalities (e.g., confocal/multiphoton microscopy, optical coherence tomography, or high-resolution ultrasound), and is capable of providing elasticity maps of specimens of sizes ranging from organoids to whole organs. Importantly, with the use of a reference hydrogel of known Young's modulus, we ensure elasticity values are reported in absolute mechanical units as opposed to reporting strains or relative stiffness.

We rigorously validate computational components of the platform, including the image registration and inverse problem solvers, before validating the combined experimental-computational framework using a hydrogel phantom with inclusions of known elastic properties. We then apply μElastography to biological

samples of fresh multicellular cancer spheroids and freshly excised murine lymph node. Our results show heterogeneous distributions of stiffness throughout 2D planes of the biological systems; spheroid stiffnesses show an average stiffness of 1.09kPa that is comparable to previous AFM measurements, while murine lymph node exhibited a range of local stiffnesses varying between ~200Pa to >5kPa in a range similar to previously reported values for murine lymph nodes, with sub-tissue features quantifiable within both biological cases. Importantly, we demonstrate not only the efficacy and application of our platform, but also the potential for our platform to democratize the stiffness measurement in the mechanobiology community: any lab with access to 3D imaging modalities (e.g., confocal microscope) could utilize this simple yet effective method to produce an elasticity map of their fresh biological sample. Such a versatile and accessible modality could be transformative in the field of mechanobiology and a valuable addition to existing elastography techniques.

2. Materials & Methods

2.1 Thermo-responsive hydrogel

A poly(*N*-isopropylacrylamide) (pNIPAAm)-based hydrogel is synthesized as previously published [36, 37]. Briefly, NIPAAm is polymerized along with *N*-(3-Aminopropyl)methacrylamide (NAPMAm) in a free radical polymerization in a molar ratio of 98:2, with potassium persulfate (KPS, 3.7mmol) and tetramethylethylenediamine (TEMED, 5.4mmol) used as initiators. The reaction mixture was chilled and purged with nitrogen gas for one hour before the flask was sealed and the reaction was left to proceed for 20 hours at room temperature, stirred at 50rpm. The resulting copolymer (p(NIPAAM-co-NAPMAm)) is purified by dialysis in excess of water for 5 days using 12-14kDa MWCO dialysis tubing. The purified product is then lyophilized. To synthesize the gel, dried copolymer is combined with NHS-Octa-PEG crosslinker (NOF America) in phosphate buffered saline (PBS) at 2.8% and 4.8% final percent solutions, respectively. Gel casts are prepared by binding polydimethylsiloxane (PDMS) wells to glass slides by plasma treatment; PDMS and glass are subjected to RF Plasma for 60 seconds before applying treated sides to one another. Completed wells are then soaked in hydrophobic agent (Rain-X Exterior Detailer and Water Repellent) for 5 minutes before being dried and continuing gel preparation. Excess liquid is aspirated from the well before gel pre-solution is pipetted in, with care being taken to not introduce bubbles. Full cross-linking occurs at room temperature (22°C) within 10-25 minutes of reagents being mixed. The crosslinked gel is submerged in PBS and removed from the cast by spatula.

2.2 Agarose Phantom Preparation

Agarose phantoms are prepared from a 1% w/v stock solution of agarose diluted to 0.5% with PBS, inert red fluorescent microparticles (Cospheric Inc, 1-5µm), and fluorescent polyacrylamide (PA) microspheres (diameter 75-150µm). PA microspheres are synthesized using previously published protocols [38] with 8% acrylamide (40% stock, Bio-rad) and 0.48% bis-acrylamide (2% stock, Bio-rad). To summarize, an oil phase comprised of kerosene (Sigma-Aldrich) and 6% w/v PGPR 4150 surfactant (Palsgaard) is prepared in a 250ml Erlenmeyer flask. PA pre-polymer solution and kerosene phase are purged separately with nitrogen gas for 15 and 30 minutes respectively. To 10ml of pre-polymer solution, 25µl of 10% w/v fluorescein o-methacrylate (Sigma-Aldrich) in dimethyl sulfoxide (DMSO) is added, followed by 70µl of 1% w/v ammonium persulfate (APS; Bio-rad) in PBS, 100µl of TEMED (Sigma-Aldrich), and 500µl of a 2% w/v stock solution of red fluorescent microparticles washed with Tween and resuspended in PBS. The pre-polymer solution is added to the oil phase and the emulsion is magnetically stirred at 600 rpm for 30 minutes. Microspheres are centrifuged and washed with kerosene multiple times to remove any remaining surfactant before being filtered to 100 – 200µm in diameter using stainless steel wire cloth (McMaster) and an excess of PBS.

Final agarose constructs are prepared in a 600µm tall layer and biopsy punched using a 1mm biopsy punch. The final phantoms consist of fluorescent red microparticles in both the agarose and PA phases,

effectively blinding the viewer to the location of the stiff PA inclusions. The location of PA inclusions is confirmed using fluorescein excitation on a separate channel. Prepared phantoms are added to a 3mm diameter PDMS well before reference agarose (1% w/v) supplemented with green fluorescent microspheres (0.0001% w/v) is pipetted around the phantom. Phantom-agarose constructs are embedded within a thermo-responsive gel such that final dimensions are 10mm in diameter and 6mm in height.

2.3 Multicellular spheroid culture

The MCa-M3C HER2/neu+ with H2B-labelled dendra2 (*Her2+, p53+*) cell line (MCa-M3C-H2B-dendra2, gift from Rakesh Jain, Ph.D.) is kept in culture at 37°C and 5% CO_2 in Dulbecco's Modified Eagle Media with L-Glutamine, 4.5g/L glucose, and sodium pyruvate (DMEM; Fisher Scientific), supplemented with 10% Fetal Bovine Serum (Gibco, 10437028) and 1% penicillin/streptomycin (Fisher Scientific). To form multicellular spheroids, cells are added to 96-well ultra-low attachment microplates (Corning) at a seeding density of 1000 cells/200µl basal media per well. Plates are centrifuged at 1200 RPM for 5 minutes using a swinging bucket rotor and incubated for 24 hours at 37°C with 5% CO_2. Following incubation, spheroids are collected from the plate using a wide-bore pipette tip and added to a 1.5ml microcentrifuge tube. For additional fluorescent contrast, Hoescht 3342 is added to a final concentration of 10µg/ml followed by incubated at 37°C and 5% CO_2 for 1 hour. Spheroids are washed with 1.5ml of DMEM prior to sample preparation.

2.4 Lymph node preparation

Healthy 10-15 week old mice are sacrificed as per protocols approved by the Institutional Animal Care and Use Committee of Boston University. Mice are from a BL6/C57 strain (Jackson Labs). Inguinal lymph nodes are dissected from surrounding tissues and rinsed in cold PBS. Tissue is embedded within sample complexes within 30-60 minutes of animal sacrifice.

2.5 Thermo-responsive sample embedding:

2.5.1 Agarose Reference

Samples are first embedded in a layer of reference agarose prior to being embedded in the thermo-responsive gel. The concentrations of reference agarose, ranging from 0.5% to 1.0%, are tailored to the expected Young's modulus of the sample: too stiff an agarose will fail to distribute compressive strains to the sample while too soft an agarose will simply deform around the sample with no compression transmitted. Reference agarose solutions are prepared with trace amounts of inert fluorescent tracers to serve as fiducial markers during the imaging and compression cycles. The size and concentration of these tracers may be optimized relative to individual sample length scales and imaging modality to ensure an adequate number of tracers within the imaging region of interest. For confocal imaging, green fluorescent polystyrene microparticles (1-5µm diameter, Cospheric Inc.) are treated with 0.1% Tween to increase hydrophilicity prior to being washed with PBS and added to agarose at a final concentration of 0.001% w/v. At the mesoscale ($\geq$ 750µm), fluorescent polystyrene microparticles (1-5µm diameter, Cospheric Inc.) are added to agarose at 0.0001% w/v.

2.5.2 Multicellular spheroid sample preparation

Spheroids are collected in a microcentrifuge tube and mixed with an equal volume of agarose (1% w/v) supplemented with fluorescent microparticles for a final reference agarose concentration of 0.5%. The agarose-spheroid compound is pipetted into a cylindrical PDMS well 4mm in diameter and 2mm tall. The complex is allowed to gel at room temperature. A 2mm biopsy punch removes a spheroid-agarose complex. Spheroid-agarose complexes are embedded within a cylindrical thermo-responsive gel with final sample dimensions of 10mm diameter and 4mm height. N = 4 spheroids were embedded, actuated, registered, and mapped.

177 2.5.3 Lymph node sample preparation

178 Harvested lymph nodes are embedded in reference agarose (0.5% w/v) supplemented with polystyrene
179 microparticles (0.0001% w/v) in a circular well measuring 4mm in diameter and 4mm in height. Tissue-
180 agarose complexes are embedded within a cylindrical thermo-responsive gel, with final sample
181 dimensions of 10mm diameter and 6mm height. N = 3 lymph nodes were embedded, actuated, registered,
182 and mapped.

183 **2.6 Experimental imaging chamber**

184 Sample complexes are submerged in PBS and sealed within PDMS wells bound to glass slides via plasma
185 treatment. Each imaging slide contains an identical control well lying parallel to the sample chamber
186 containing an internal ultra-thin 10K thermistor (Adafruit Inc) for monitoring chamber temperatures via
187 an Arduino board connected to a local computer. The imaging slide is placed within a custom-designed,
188 3D-printed (Stratasys) sample holder. The top and bottom faces of the sample holder have windows that
189 allow for excitation light to pass through unobstructed, thereby permitting use with multiple imaging
190 modalities. Within the sample holder, a milled aluminum water chamber with a glass top and bottom is in
191 direct contact with the sample, connected via tubing to an external radiator submerged in a heated water
192 bath for controlled heat application.

193 **2.7 Microscopy parameters**

194 For all samples, images are taken at room temperature before the system is heated. Checkpoint images are
195 taken throughout the heating cycle to verify sample integrity and gradual ongoing compression. Final
196 compressed images are taken at 35-37°C.

197 2.7.1 Imaging agarose phantom with laser scanning confocal microscopy

198 Phantom validation images are acquired using an Olympus FV3000 laser scanning confocal microscope
199 using a UPLSAPO10X2 (Olympus, NA 0.4, 10x magnification) air immersion objective lens with 1.5x
200 optical zoom applied. The bulk phantom is excited using 561nm laser excitation (0.05% transmissivity,
201 TexasRed channel), and surrounding reference agarose is excited using 488nm laser excitation (0.1%
202 transmissivity, FITC filter). Images are taken using Resonant scanning mode with 4x line averaging to
203 increase signal. The final phantom image (1019x1019 pixels) was comprised of 4 subimages (512x512
204 pixels, scanning voxels of 1.6573x1.6573x5μm^3) stitched together using Olympus software. Images are
205 cropped and projected to single 8bit channel image stacks using FIJI (ImageJ).

206 2.7.2 Imaging multicellular spheroids with laser scanning confocal microscopy

207 Multicellular spheroids are imaged using an Olympus FV3000 laser scanning confocal microscope using
208 a UPLSAPO10X2 (Olympus, NA 0.4, 10x magnification) air immersion objective lens with 5x optical
209 zoom applied. Green nanoparticles in the agarose phase are excited with 488nm laser excitation (1%
210 transmissivity, Alexa 488 channel) and the spheroid is excited with 405nm excitation (8.5%
211 transmissivity, Hoescht 33258 channel). Images were 512x512 pixels with scanning voxels of
212 0.4972x0.4972x2.56μm^3 taken with Galvano scanning mode.

213 2.7.3 Imaging murine lymph node with optical coherence tomography

214 Lymph nodes are imaged on a commercial spectral-domain OCT system with ThorImage OCT software
215 (Thorlabs) with 10x air objective (Mitutoyo, 0.28 NA). The light source was a broadband
216 superluminescent diode with center wavelength of 1300nm and a full width half maximum bandwidth of
217 150nm. Images were taken with 2.6μm pixel resolutions in X, Y, and Z, and scanning resolution of
218 ~1250x1250x200 pixels in X, Y, and Z respectively.

219 **2.8 Image Registration and Kinematic Calculations**

Relaxed and compressed image sets are processed using a previously published deformable image registration algorithm [32, 33]. Briefly, multi-channel images are merged into a single channel, 8-bit image stack using ImageJ. Validation phantom and spheroid images are upsampled along the depth axis to generate data with isotropic voxels. Processed files are stored as *nii.gz* format and passed to image registration software along with an affine transformation matrix that serves as an initial approximation of the displacement map. The registration software, written in C++11 and Matlab (version 2022b), models the registration problem as inference on a Markov Random Field (MRF). The algorithm performs belief propagation at successively finer resolutions to determine the latent displacements necessary to minimize the dissimilarity between the registered images; for each iteration of the algorithm, search parameters include the grid spacing (G) between control points in the MRF, the quantized magnitude of the sampled displacements (Q), and the maximum search radius (L) specified in units of Q [32, 33]. For our processing, the optimal values of the G, L, and Q parameters varied depending on the degree of strain seen between images. Typical values for G, L, and Q were [8 4 2 1].

The algorithm outputs a nonlinearly transformed image that is compared to compressed target images to evaluate goodness of fit. The algorithm also produces a nonlinear displacement field; a variety of canonical strain tensors, areal strain maps, and volumetric strain maps can be calculated via use of a cubic smoothing spline to reduce noise in the displacements (Supplemental Figure 1). The Cauchy strain field is calculated from the smoothed displacement field as follows:

$$\varepsilon = \frac{1}{2}(\nabla u + (\nabla u)^T)$$

By definition, areal and volumetric strains are computed as the trace of the Cauchy stress tensor (i.e., $\varepsilon_{xx} + \varepsilon_{yy}$, $\varepsilon_{xx} + \varepsilon_{yy} + \varepsilon_{ZZ}$ respectively). It is important to note that the areal strain does not represent the strain along a single axis; images presented here show the summation of strains along both axes of a particular pixel. As an example, a pixel shown to undergo a 50% areal strain would in reality experience a combination of strains totaling 50% along the X and Y-directions, instead of a linear 50% strain along X and an additional linear 50% along Y. Typical values for these directional strains ε_{xx} and ε_{yy} are in the range of -0.1 to -0.3.

Deformation fields may be smoothed to varying degrees using a cubic smoothing spline interpolation to remove remaining noise artifacts following registration; the smoothing function (*csaps,* Matlab) takes an input argument for the smoothing parameter *p* to define the distance between the data's fit and a cubic spline interpolant. The value *p* lies in the range [0,1] where smaller values of *p* indicate a higher degree of smoothing.

2.9 Inverse Problem Solving

Displacement fields generated by image registration are input into a customized adjoint-weighted variational equation (AWE) formulation of the inverse problem [34, 35] written for the FeniCS finite element modeling (FEM) platform (v2019.1.0, run via Ubuntu for Windows). Briefly, the AWE algorithm determines the scalar shear modulus field, $\mu(\boldsymbol{x})$, that minimizes the error in the Cauchy equilibrium equation and whose stiffness is constrained to match the Young's modulus of the reference agarose on the boundary of the domain. Input deformation fields are cropped to fit the sample boundary; cropping also helps remove artifacts from the affine transform performed within the image registration. In 2D, a 250x250 mesh is defined across the input data. Displacement values in each dimension are interpolated at the mesh vertices. Poisson's ratio of 0.36 (Supplemental Figure 2) is assumed for a compressible, linearly elastic sample.

Stresses are calculated by expressing the Cauchy stress tensor $\boldsymbol{\sigma(x)}$ as the product of an unknown scalar shear modulus field $\mu(\boldsymbol{x})$ and a second-order tensor $\boldsymbol{A(x)}$, which is a function of the deformation gradient tensor and whose form depends on the particular constitutive equation:

$$\boldsymbol{\sigma}(\boldsymbol{x}) = \mu(\boldsymbol{x})\boldsymbol{A}(\boldsymbol{x})$$

Here, $\mu(\boldsymbol{x})$ is an unknown value solved for by satisfying the equilibrium equation:

$$\nabla_{\mathrm{x}} \cdot \boldsymbol{\sigma}(\boldsymbol{x}) = 0$$

The known elastic modulus for agarose is used as a reference for calibration purposes and is enforced as a Dirichlet boundary condition on the modulus by prescribing values of $\mu(\boldsymbol{x})$ on the boundary of the domain when calculating the equilibrium solution [35]. The system is solved to calculate the elasticity values within the mesh. Output files are converted to *.csv* format (Paraview) before further processing and visualization (Matlab); we utilize the Matlab file function *inpaint_nans* to remove NaN values from data import. Further formulation can be found in Supplemental Information.

2.10 Measurement of agarose Poisson's ratio

Compression tests were performed on 10mm diameter biopsy punch from a 5mm tall agarose gel (1% w/v) supplemented with fluorescent tracers (0.0001% w/v). The biopsy punch was placed on a glass slide with a glass coverslip on its top face, and a compressive strain of approximately 5-10% applied via a manually lowered compressive arm (Supplemental Figure 2). Images of the agarose before and after compression were taken using a stereomicroscope coupled with NightSea fluorescent excitation lamp. A total of 12 measurements were taken with N = 2 agarose biopsies (m = 5 and m = 7 respectively). Between measurements, strains were relieved and agarose was allowed to equilibrate in PBS for 5 minutes. Poisson's ratio was calculated by taking the negative ratio of lateral strain (expansion) to linear strain (compression).

2.11 AFM-based measurement of Young's modulus

Young's modulus values for agarose references, agarose phantom bulk phase, and PA beads are obtained using an Asylum MFP3D atomic force microscope (AFM). Polystyrene colloidal probe tips of radius R ~ 26μm (Polysciences) were attached to tipless cantilevers by UV cured glue. For each measurement, the exact spring constant *k* of the cantilever was directly measured using a thermal calibration method [39]. Each sample was indented 4-5 times and the resulting displacements *d* are translated to force *F* using Hooke's Law ($F = kd$).

For PA spheres of radius *R*, experimental loading force-displacement curves are fit to Hertzian contact mechanics models using:

$$F = \frac{4}{3} E_{ind} \left(\frac{R_1 R_2}{R_1 + R_2} \right)^{\frac{1}{2}} * \frac{(d_{total})^{\frac{3}{2}}}{1 + \left(\frac{R_1}{R_1 + R_2} \right)^{\frac{1}{3}}}$$

where R_1 is the radius of the spherical colloidal probe tip, R_2 is the sphere radius, and d_{total} is the indentation depth.

In the case of flat agarose samples, E_{ind} is calculated using [40]:

$$F = \frac{4}{3} \frac{E_{ind}}{(1 - \nu^2)} {R_1}^{1/2} * (d_{total})^{3/2}$$

where ν is the Poisson's ratio of the agarose: 0.36.

2.12 Stress relaxation characterization of agarose

Unconstrained compression tests are performed on 0.5% (w/v) agarose with dimensions of 2mm (height) by 6mm (diameter) using a commercially available Instron 5944 Micro-tester. Hydration was maintained via PBS, though excess liquid was aspirated from the agarose prior to test initiation. Using a 5N load cell, stepwise 5% (0.1mm) strains are applied to the agarose over the course of 1 second, each followed by a 3-5 minute equilibration and force measurement period. Stress is calculated from force response curves of n = 3 gels with a total of 15% - 20% strain applied; stress-time curves for each stepwise strain are fit to an exponential to find the time constants τ. Time constants are then grouped by response timescale (i.e., short versus long timescale) and averaged within each gel. The average short term time response constant was 8.09s. The average long-term response constant was 150.2s.

$$\sigma(t) = a * \exp\left(-\frac{t}{\tau_1}\right) + b * \exp\left(-\frac{t}{\tau_2}\right)$$

2.13 Histology of fixed lymph nodes

Lymph nodes are prepared for histology as follows: n = 2 lymph nodes are dissected from sacrificed mouse and embedded in experimental complex (reference agarose within thermoresponsive gel). Samples are heated and compressed before being dissected from thermoresponsive gel and reference agarose; as a control for any damage that occurs during the act of embedding and sample preparation, an additional n = 2 lymph nodes are fully embedded but not compressed. They are kept at room temperature in PBS for the duration of the heating and compression experiments (60 minutes). Samples are fixed overnight in 10% formalin buffered solution before being washed three times with cold PBS and stored at 4°C. Histology slicing and hematoxylin and eosin staining is performed by the Boston University Collaborative Research Laboratory (CoRE).

2.14 Validation of AWE formulation for a linearly elastic material

A 200x200 square was generated in ABAQUS (Dassault Systèmes, v CAE 2019) using element type CPS4R, a four-node plane stress element, with 441 nodes. The square was partitioned into the inner 10x10 elements of the mesh grid, and the remaining outer edge elements. The outer and inner partitions were assigned elastic material properties in the following combinations [outer Young's modulus (kPa), inner Young's modulus (kPa)]: [5,10], [5, 25], [5, 50], [5, 2.5]. Each material was assigned a Poisson's ratio of 0.3. The center point was set with an ENCASTRE boundary condition. A 10% linear displacement was applied to each edge of the square towards the opposite edge. All of the node displacements were output as *.rpt files.

Given the positions of the nodes in the original configuration, $\boldsymbol{X}$, and in the deformed configuration $\boldsymbol{x}$, the displacement map in the spatial configuration was calculated as $\boldsymbol{u}(\boldsymbol{x}) = \boldsymbol{x} - \boldsymbol{X}(\boldsymbol{x})$. To validate the inverse solver, this map was subsequently passed as input to the inverse solver, and the estimated elastic modulus was compared to the ground-truth elastic modulus.

Additional mapping was performed to ensure validation using a more complex sample. A 20x20 square geometry was generated in ABAQUS (Dassault Systèmes, v CAE 2019). This square geometry was then partitioned with a large circle centered on the square's centroid and having diameter 10; this region was then partitioned with four smaller circles each having diameter 2. The final geometry was then meshed using element type CPS4R with 8122 nodes. The subdomains were assigned elastic material properties such that [outer Young's modulus (kPa), Young's modulus inside large circle (kPa), Young's modulus inside small circles (kPa)] = [5, 10, 15]. Each material was assigned a Poisson's ratio of 0.36. The top edge of the domain was constrained to prevent vertical translation, while the left edge was constrained to prevent horizontal translation. The bottom was displaced upward by 10%, while the right edge was

displacement leftward by 10%. All of the node displacements were output as *.rpt files. Gaussian white noise was applied to the output deformation field; noise distributions had a mean of 0 and variances ranging from 1E-7 to 1E-4 in steps of 1E-1. Original and noised maps were then input into the inverse solver both as is and after being smoothed with a cubic smoothing spline (*csaps,* Matlab, smoothing factor 0.01), and the maps of elastic modulus were compared to the ground truth data.

2.15 Validation of Image Registration Deformation fields & Strain

A displacement map $\mathbf{u_k}(\mathbf{x})$ of the following form corresponds to a spherically symmetric contraction or dilation about a given point in space:

$$\boldsymbol{u_k}(\boldsymbol{x}) = A_k\left(1 - \exp\left(-\frac{\boldsymbol{r}(\boldsymbol{x})^2}{\sigma_k^2}\right)\right) * \exp\left(-\frac{\boldsymbol{r}(\boldsymbol{x})^2}{\sigma_2}\right) * \boldsymbol{r}(\boldsymbol{x})/||\boldsymbol{r}(\boldsymbol{x})||$$

where $\mathbf{u}(\mathbf{x})$ is the displacement vector at the point $\mathbf{x}$, $\mathbf{r}(\mathbf{x})$ is a position vector measured from the center of dilation to the position $\mathbf{x}$, and $\mathbf{x}$ is any position in the domain. The parameters A_k and σ_k control the amplitude and the falloff of the displacements, respectively. To validate the image-registration algorithm and subsequent strain computations, an image from the phantom-validation experiment was deformed using a synthetic, ground-truth displacement map of the form $\mathbf{u_{GT}}(\mathbf{x}) = \mathbf{u_1}(\mathbf{x}) + \mathbf{u_2}(\mathbf{x})$, where the parameters A_1, A_2, σ_1 and σ_2 were chosen to produce areal strains up to ±10% centered on two regions of the xy-plane where there are phantom inclusions. The areal strain is the trace of the Cauchy strain tensor. The image-registration algorithm was then used to recover an estimation of these ground-truth displacements, $\mathbf{u_{measured}}(\mathbf{x})$.

Owing to noise in the registered displacements, we found it to be advantageous to subsequently smooth these displacements with a cubic smoothing spline (Matlab, *csaps*), the degree of smoothness of which is controlled by a regularization parameter *p* responsible for penalizing curvature in the output. For different values of this smoothing parameter, the ground-truth displacements and strains were finally compared to the measured displacements and strains. During these validation tests, the optimal value of the smoothing parameter was found to be at an intermediate value near 0.001.

2.16 Comparison of agarose maps

Two agarose samples of 0.5% and 1.5% w/v are cast in 1mm diameter x 1 mm height disks and embedded within separate 1% reference agarose gels of 3mm diameter x 2mm height. 0.5% agarose is supplemented with blue fluorescent polystyrene microparticles (1-5µm diameter), 1.5% agarose is supplemented with red fluorescent polystyrene microparticles (1-5µm diameter), and 1% reference agarose is supplemented with green fluorescent polystyrene microparticles (1-5µm diameter); all are at an equal concentration of 0.0001% w/v. Imaging took place using an Olympus FV3000 laser scanning confocal microscope with UPLSAPO10X2 10x objective (N.A. 0.4) and excitation lasers of 405nm (0.5% Agarose), 488nm (1% Agarose), and 561nm (1.5% Agarose) with imaging channels for DAPI, Alexa 488, and Texas Red respectively. Laser transmissivities were set between 0.5 and 1% total power, with photomultiplier voltages set to 500. Image slices were 512x512px^2 with voxels of size 2.4859x2.4859x5 µm^3. Files were upsampled in Z to create isotropic voxels prior to registration and subsequent analysis. For statistical comparison, maps were randomly sampled at 6 points using a mask created from PA inclusions used during phantom validation as a consistent functional unit.

2.17 Statistical Analysis

Values where presented are mean values +/- standard error unless otherwise noted. Statistical tests for significance are performed using a two-tailed Student's t-test assuming equal variance. Comparison between AFM model of phantom stiffness with µElastography phantom stiffness is performed by

discretizing the μElastography-generated, segmented elasticity map into smaller discrete units. PA inclusions are segmented out and averaged between inclusions. For phantom body and reference gel, N = 6 data points are gathered for each phase by sampling areas that are equal to an average inclusion area.

3. Results

3.1 Development of 3-D temperature responsive system for mechanical characterization

We have designed and implemented a hydrogel-based μElastography platform for the characterization of biological sample elasticities via multi-directional mechanical perturbation (Fig. 1a). The μElastography platform employs a biocompatible, thermo-responsive hydrogel to apply small (typically up to 10%), multi-directional compressive strains to an embedded sample. We capture the sample deformation by high resolution optical microscopy and derive the internal elastic properties by computationally solving the inverse problem. Our method generates absolute elasticity measurements instead of relative quantifications by surrounding the sample of interest with a reference hydrogel of known Young's modulus *E*.

To prepare the platform for mechanical actuation, biological samples with internal fiducial markers are surrounded by a reference layer of agarose supplemented with micron-scale fluorescent tracers; fiducial markers may be tissue features or fluorescently labeled cells. The sample-agarose complex is then embedded within a p(NIPAAm)-based thermo-responsive hydrogel (Fig. 1b, Fig 1d, Supplemental Figure 3). At room temperature (22°C), the gel remains in a relaxed, un-stressed state; at elevated temperatures (>35°C), the cross-linked polymers undergo a reversible coil-globule transition and collapse, resulting in gel contraction (Fig. 1c, Fig. 1d). We are able to embed a variety of biological samples within the gel and tailor fluorescent tracers to avoid fluorescent cross-talk (Fig. 1d); without an embedded sample, the heating-induced contraction can result in up to 20-30% reductions in diameter (Fig. 1e). We tailor heating profiles to sample size and type, typically applying a gradual ramp over 20 – 60 minutes (Fig. 1f).

As agarose hydrogels are known to exhibit poroelastic behavior, whereby fluid flow through the pores of the solid agarose scaffold influences the mechanical response of the scaffold to strains, we verify that our perturbation lies outside this poroelastic regime by measuring the stress relaxation time constant of an agarose hydrogel with similar or larger diameters than used in our platform under a 10% compressive strain (Fig. 1g); we find short- and long-term relaxation time constants of 8 and 150 seconds, respectively. As these relaxation constants are a factor of 12 smaller than our shortest heating duration, we can assume that the measured strain response of the agarose-sample complex reflects the equilibrium elastic material properties only, and not the time-dependent poroelastic properties of agarose. It is important to note that although the thermo-responsive gel can predictably undergo 20-30% reductions in diameter, the embedded sample does not experience this degree of compaction; rather, embedded sample constructs typically only experience $\leq$10% reductions in diameter. Smaller gel strains can be achieved by heating the gel to a lower temperature or incubating for shorter time periods [37] (Fig. 1h).

It is known that temperature can dictate tissue mechanical properties [41], yet some variation remains within the biomechanics community as to what temperature mechanical measurements should be performed at: whether room temperature [4, 31, 42-45] or at/near physiological temperature [46, 47]. Some studies cite the necessity of temperature maintenance to prevent tissue degradation or stiffness artifacts at lower temperatures [41, 46], but there are fewer studies that focus on the direct effect of heat ramp and mechanical changes. However, it is worthwhile to note that a previously published method employing deformable hydrogel probes to measure local stiffness in biological samples utilized a similar proposed temperature range (37°C to ~20°C) [31]. Thus, while not anticipated to be a major problem, in the event of a sample that is highly sensitive to temperature changes, we can instead focus the temperature

change to a tight range around the thermo-responsive gel transition temperature (e.g., between 33°C and 37°C).

The experimental system is contained within a PDMS imaging chamber affixed to a glass slide and sealed with a coverslip to create a closed system for heating and imaging purposes (Fig. 1i); the system design enables both upright (e.g., common in two-photon and optical coherence tomography) and inverted imaging (e.g., confocal microscopy) and is easily adaptable across microscope modalities (Supplemental Figure 4). Heat is applied to the system by exposing the sample chamber to circulating water from a heat reservoir. An identical well parallel to the specimen well holds a thermistor linked to external Arduino interface for monitoring chamber temperature.

Images of the sample in the relaxed and compressed states are acquired and input into a deformable image registration algorithm [33], using a generalized affine transformation coupled with nonlinear deformations to generate a registered output image that matches the compressed image. The image registration process also results in a detailed 3D deformation field that recaptures the movement of the sample in X, Y, and Z as it is compressed by the thermo-responsive gel. We validate the application and accuracy of the image registration software, as well as the effect of various degrees of smoothing on the data, by applying known deformations and strain values to an image and comparing the known values to the registration results (Supplemental Figure 1).

We then solve the inverse problem using registration-produced deformation fields to generate elasticity values. Boundary conditions for solving this problem are determined by the reference agarose (Fig. 1j): fluorescent tracers added to the reference hydrogel serve as a fiducial marker to improve image registration accuracy and simultaneously enable detailed quantification of reference agarose deformation. Furthermore, as the Young's modulus of the agarose is quantified *a priori* by way of AFM, its use as a boundary condition ensures absolute estimation of the elasticity of the specimen of interest. In formulating the solution to the inverse problem, we first utilize a linearly elastic, compressible model of the adjoint-weighted variational form [34, 35]. A detailed formulation of this solver may be found in Supplemental Information. To verify the use of this model and solver for our application, we first validate its efficacy using finite element model (FEM) simulations consisting of a linearly elastic sample material embedded within a linearly elastic reference material (Supplemental Figure 5). The Young's Modulus of the sample was varied relative to the Young's Modulus of the reference material, and the entire system underwent 10% compressions to each face. We find that with this simple boundary condition enforced, the solver is able to detect the sample shape and comparable elasticity values. Our validation further shows the presence of an optimal window of reference Young's modulus relative to the interior sample, whereby accuracy decreases if the reference gel is too soft compared to the interior sample; this relationship supports the importance of choosing correct reference hydrogels for the samples being investigated. To ensure our solver was compatible with more complex samples, we generated an additional FEM simulation of a linearly elastic sample material within linearly elastic reference (Supplemental Figure 6); in this case, the circular sample had embedded circular mechanical heterogeneities. To further evaluate the system's capabilities, we applied varying degrees of noise to the simulated deformation fields before smoothing this data as per our computational pipeline. The resulting elasticity maps not only recapture the interior heterogeneities of this synthetic sample, but also demonstrate the capability of our pipeline to successfully detect signal from otherwise noise-filled data.

Using readily available reagents and fluorescent microscopy, this highly scalable experimental design enables precise control of multi-directional mechanical actuation and results in detailed spatial maps of live tissue elastic properties. This platform is biocompatible and may be applied across a range of

biological length-scales and imaging modalities (Fig. 1k, Supplemental Figure 4) to generate absolute elasticity values without the need of AFM or other specialized equipment.

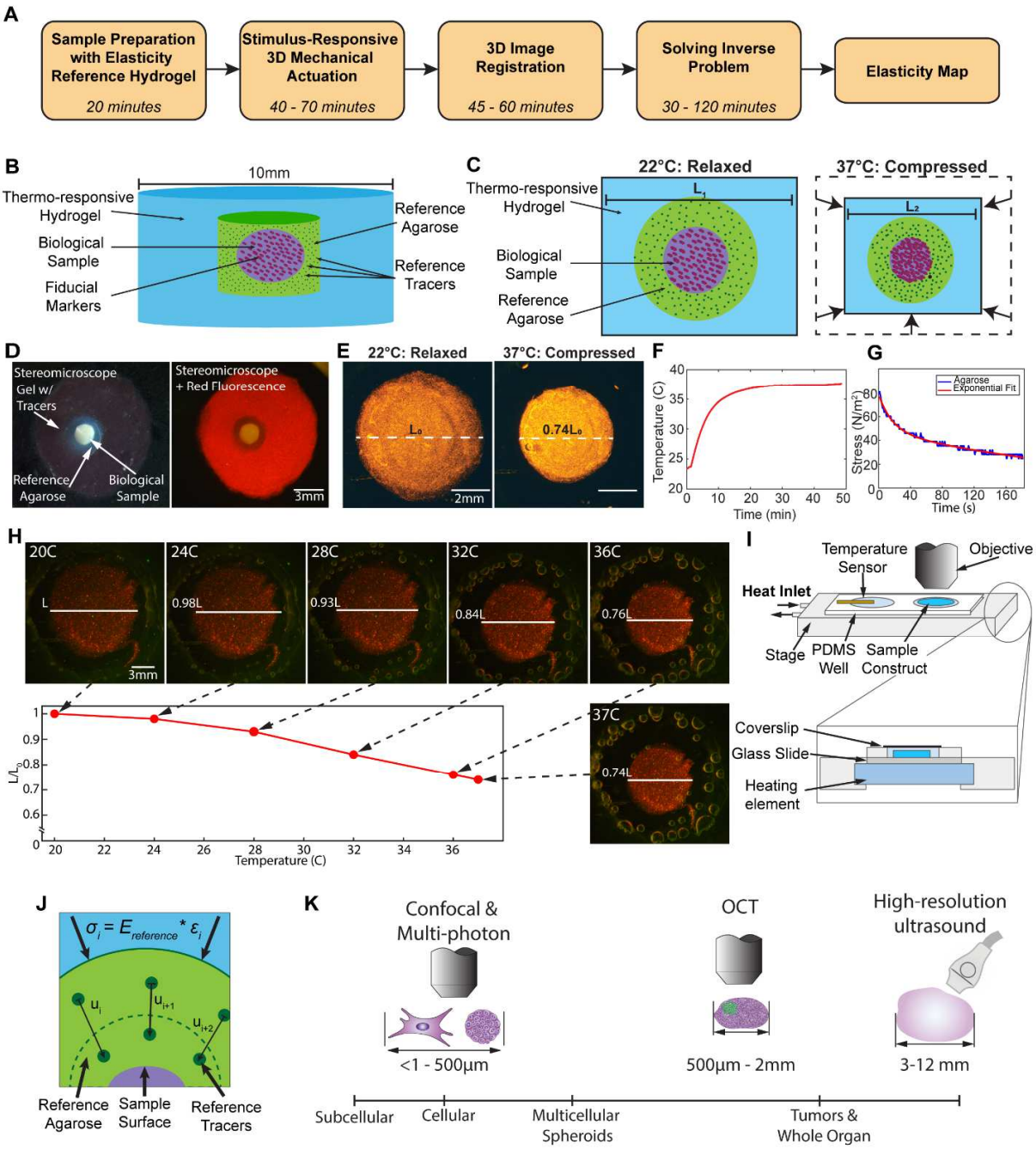

3.2 Validation of Heterogeneity detection using hydrogel phantom

To validate our platform's ability to detect elastic heterogeneities within a sample, we first map the stiffness distribution of a composite hydrogel phantom. The 1mm diameter phantom consisted of 0.5% agarose measured by AFM to be 2.6 kPa $\pm$ 0.1kPa with stiff polyacrylamide (PA) microspheres embedded randomly throughout its 500µm height (Fig. 2a, 2b) that served as internal mechanical heterogeneities; PA microspheres were approximately 75-150µm diameter and were measured by AFM to be 29.3kPa $\pm$ 2.3kPa. Phantom agarose and PA spheres were both supplemented with red fluorescent

microparticles as fiducial tracers (Fig. 2b, magenta); reference agarose was supplemented with an equal concentration of green fluorescent microparticles. To enable identification of PA microspheres, microspheres were additionally labeled with fluorescein for bulk sphere fluorescence in a separate channel (Fig. 2b, interior green circles), though at a negligible enough concentration to not interfere with microparticle excitation. The individual Young's modulus values of the final prepared agarose (2.6kPa $\pm$ 0.10kPa) and PA microspheres (29.3kPa $\pm$ 2.27kPa) are presented in Table 2: the embedded PA inclusions represent approximately a 10x increase in sample elasticity.

The phantom was embedded in reference agarose supplemented with green fluorescent microparticles (Fig 2b); the Young's modulus of this reference hydrogel was measured by AFM to be 7.8 kPa $\pm$ 0.25kPa. The system was heated to 37°C and equilibrated for 30 minutes before images of the compressed samples were acquired. Single plane images taken in the relaxed (Fig. 2b(i)) and compressed (Fig. 2b(ii)) states show 10-20% compressive strains in the X-Y plane. Deformable image registration software generated a deformed image stack (Fig. 2c) that recaptures the distribution of fiducial markers throughout the phantom 2D plane, including the slight aberrations that align with internal PA microspheres (Fig 2c, annotated circles). Due to affine-transform induced edge effects, image matrices were cropped for further analysis (Fig. 2c, annotated square). Sample curves taken during the AFM measurements of phantom components (Fig. 2d) highlight the substantial difference in mechanical responses of phantom components that should manifest as stiffness heterogeneities.

The registration process also produces a 3D deformation field between relaxed and registered states at optical resolution (Fig. 2e). Cauchy stress components of the phantom deformation (Fig. 2f(i,ii,iii)) clearly show heterogeneities in stress that correspond to inclusion locations in their X- and Y-components, though z-components are less obvious than their counterparts. Areal strain of a 2D plane (Fig. 2f(iv)) of the registered image shows the overall compression (negative strain, cool colors) experienced by the system punctuated by sharp peaks of near zero (warm colors) that correspond to PA microsphere location; here, it is important to recall that the areal strains calculated represent the summation of strains in the X- and Y-directions, and their magnitudes do not represent an equal, isotropic strain across both X- and Y-axes. Further analysis of deformation fields produces shear components of the Cauchy stress (Fig. 2f(v,vi,vii)). Finally, a volumetric strain analysis (Fig. 2f(viii)) recaptures peaks of near zero strain corresponding to sphere location, similar to the areal counterpart.

Stiffness values are calculated in this 2D plane by solving the inverse problem with the Young's modulus of reference agarose used as boundary condition. The resulting stiffness map captures the location of beads within the phantom agarose as characterized by high peaks in elasticity (Fig 2g, warm colors). As some regions of the areal strain map exhibited elevated (i.e., >40%) linear strains, we further apply a nonlinear, hyper-elastic neo-Hookean version of the inverse problem (Fig. 2h). To evaluate the accuracy of both of our methods, we compare these elasticity values obtained by µElastography to the Young's modulus of each component obtained via AFM (Fig. 2h) using masks manually segmented from fluorescent data; the same masks are used to calculate values for average phantom body, PA inclusion, and reference agarose elasticities from the 2D elasticity map and compare with AFM values (Fig. 2j, Fig. 2k). Our methods calculate statistically similar mean elastic modulus values for reference agarose in the linear ($E_{\text{Linear, Reference}}$ = 7.6kPa $\pm$ 0.32kPa) and nonlinear ($E_{\text{Nonlinear, Reference}}$ = 8.41kPa $\pm$ 0.65kPa) cases, while the nonlinear solver performs better at recapturing the elasticity of embedded inclusions ($E_{\text{Nonlinear, PA}}$ = 32.17kPa $\pm$ 5.1kPa) compared to the linear solver ($E_{\text{Linear, PA}}$ = 16kPa $\pm$ 1.92kPa). Both solvers overestimate the stiffness of the body of the phantom ($E_{\text{Linear, Body}}$ = 6.1kPa $\pm$ 0.24kPa, $E_{\text{Nonlinear, Body}}$ = 5.97kPa $\pm$ 0.37kPa). Values are summarized in Table 2. To verify that the act of smoothing does not introduce artifacts in the downstream deformation maps, we quantify the distribution of values at varying

smoothing values (p = 0, 0.1, 0.01, 0.001) and compare the modes of the distributions, finding highly similar distributions between the 4 smoothing values (Supplemental Figure 7). To offer additional support to our method, we characterize two additional samples of agarose (0.5% and 1.5% w/v, Supplemental Figure 8). Here, we see a notable shift in the values calculated by μElastography: 6.09kPa $\pm$ 0.29kPa and 10.19kPa $\pm$ 0.18kPa. Comparing these values to AFM measurements for similar agarose formulations, we see similarity between the 1.5% agarose stiffnesses, with an average AFM measurement of 15.5kPa $\pm$ 2.95kPa. While there remains a difference between the softer samples, this discrepancy between the values measured via AFM and μElastography as well as the differences observed within the phantom agarose may be explained by key differences between the methodologies. In addition to the complexities of sample heterogeneities that may not be captured via 2D AFM and the differing nature of 2D vs 3D measurements, the fundamental methods of elasticity measurement are different: in AFM, the Young's modulus is derived from the indentation modulus through the Hertzian model, which usually results in discrepancies between AFM and macroscale stiffness measurement methods such as confined and unconfined compression tests. Our method instead relies upon solving the inverse problem. Importantly, while the μElastography results may not align perfectly with AFM measurements, the results of both nonlinear and linear formulations of the inverse problem recapture significant differences between groups. Thus, our method here is capable of capturing the complex heterogeneities of the material, including subtle, site-specific variations in internal mechanical properties otherwise absent within averaged bulk AFM measurements.

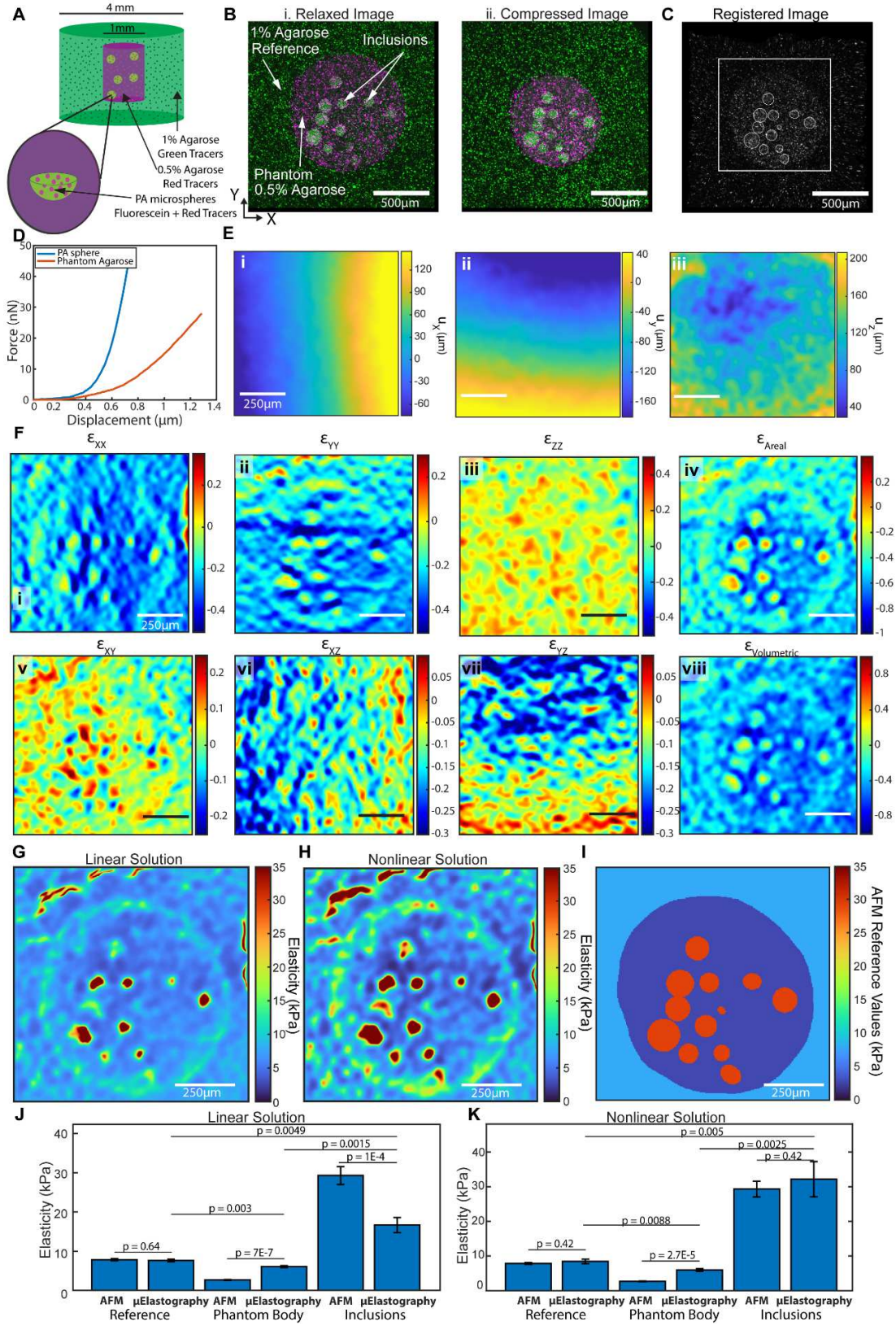
A
4 mm
1mm
1% Agarose
Green Tracers
0.5% Agarose
Red Tracers
PA microspheres
Fluorescein + Red Tracers
B
i. Relaxed Image
1% Agarose
Reference
Inclusions
Phantom
0.5% Agarose
500µm
ii. Compressed Image
500µm
C
Registered Image
500µm
D
PA sphere
Phantom Agarose
Force (nN)
Displacement (µm)
E
i
ii
iii
250µm
F
ε_{XX}
ε_{YY}
ε_{ZZ}
ε_{Areal}
ε_{XY}
ε_{XZ}
ε_{YZ}
$\varepsilon_{Volumetric}$
250µm
G
Linear Solution
H
Nonlinear Solution
I
Elasticity (kPa)
AFM Reference Values (kPa)
250µm
J
Linear Solution
p = 0.0049
p = 0.0015
p = 1E-4
p = 0.003
p = 0.64
p = 7E-7
Elasticity (kPa)
AFM µElastography AFM µElastography AFM µElastography
Reference Phantom Body Inclusions
K
Nonlinear Solution
p = 0.005
p = 0.0025
p = 0.42
p = 0.0088
p = 0.42
p = 2.7E-5
Elasticity (kPa)
AFM µElastography AFM µElastography AFM µElastography
Reference Phantom Body Inclusions

549

3.3 Elastic characterization of murine multicellular cancer spheroid

We next demonstrate elastic characterization of live tissue by mapping the internal elasticity distribution of a live multicellular cancer spheroid. A live, ~1000-cell spheroid is embedded within reference agarose supplemented with micronscale fluorescent tracers and imaged via spinning disk confocal microscopy (Fig. 3a(i)). The sample undergoes 2-15% linear strains upon heat-induced gel compression (Fig. 3a(ii)). Image registration deforms the images from the relaxed original state to the compressed target image (Fig. 3b) across the entire volume of the spheroid; here, we focus analysis on one 2D plane.

Full 3D deformation field are smoothed using a smoothing parameter of 0.01 to eliminate noise artifacts (see Methods) and are then used to calculate areal strain maps (Fig. 3c). Regions of higher positive strain (warm colors) punctuate the 2D plane of the sample, balanced by more extreme negative, compressive strain (cool colors) local and at the edge of the spheroid. Calculating the 2D linear elasticity map from the smoothed deformation fields generates a heterogeneous map of the internal elastic properties of the spheroid, with boundary of spheroid-agarose clearly visible (Fig. 3d). Within a single XY plane, peaks of stiffness arise around groups of cells, while the majority of the spheroid remains in a softer regime. To offer further quantification, particularly due to the regions of highly negative strain in Figure 3c, we additionally solve for spheroid elasticities using a nonlinear solver (Fig. 3e). Normalized histograms of elasticity values (Fig. 3f) exhibit similar trends between solvers.

Across the spheroids quantified, we find an average elasticity of 1.09kPa $\pm$ 0.9kPa within the linear case, and 1.45kPa $\pm$ 1.3kPa in the nonlinear case. These values align with previous AFM measurements from our lab that found similarly sized spheroids to exhibit a Young's modulus of 0.9 $\pm$ 0.13kPa (Fig. 3g) [48]. The wide standard error of the mean stiffness values may arise due to variations in exact culture time and condition; furthermore, previous AFM studies found a wide range of intracellular stiffnesses of single cells (from 380Pa – 5kPa [48-50]) depending on measurement location. Thus, the variation in the values measured via our method may align with these intracellular variations. Highly heterogeneous and unexpectedly high levels of localized intraspheroid stiffness have been previously reported using intraspheroid probes [31], yet the spatial information of these and most popular *in vivo* elasticity measurements is limited to the local environment of the stimulus [30, 31]. Our measurements here illustrate the ability of μElastography to resolve stiffness at suborganoid scale via spatial maps.

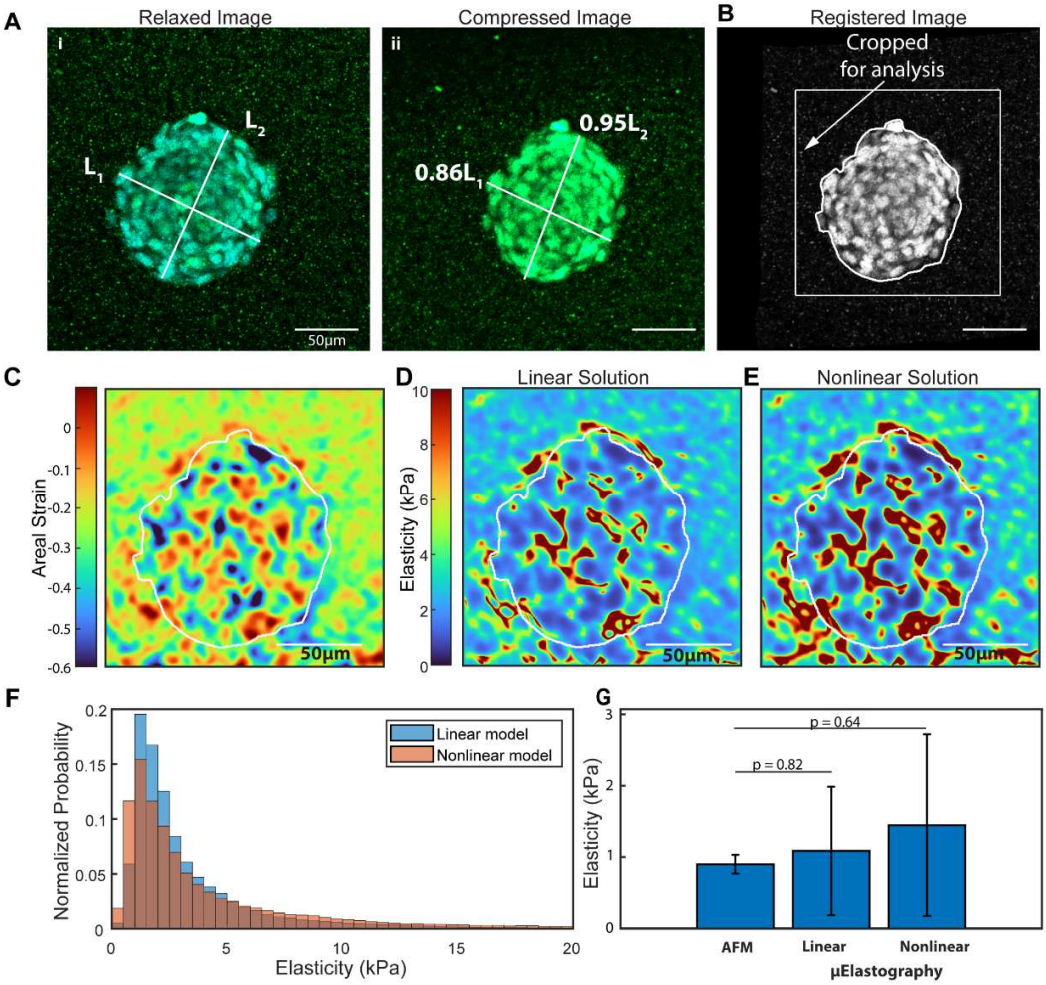

3.4 Elasticity mapping of murine lymph node

To evaluate the platform's capabilities at the whole tissue scale, we embed and actuate a fresh murine inguinal lymph node and map the interior elastic properties of the intact organ. Upon thermally actuated compression, embedded lymph node tissue experienced linear strains of approximately 7% in the XY plane (Fig. 4a, 4b). Though the entire area of the tissue (2.4mm^2) was imaged in the Z direction, image stacks were cropped to a 46 slice (~120μm) depth in Z to focus analysis on a highly excited, in-focus range of tissue. Image registration was performed to generate a deformed image (Fig. 4c) that aligns well with raw data.

Areal strain maps (Fig. 4d) are calculated using registration-produced deformation fields cropped to tissue boundaries (Fig. 4c Annotations). Quantification generates regions of negative strain within the tissue border (cool colors) and more positive strain exterior to the tissue bounds (warm colors). The majority of the tissue interior experiences slightly negative strains, though pockets of highly negative strain punctuate throughout the interior of the tissue. To ensure that the sample preparation and application of large strains during tissue compression does not result in permanent tissue damage, hematoxylin and eosin (H&E) staining was performed on control and compressed lymph nodes. The H&E staining of the tissue (Supplemental Figure 9) shows no impressionable differences in cell morphology or tissue structure between the compressed and control cases.

A total of 3 lymph nodes are mapped and characterized, reporting an average stiffness of 0.64kPa ± 0.08kPa when quantified with the linear solver (Fig. 4e), and 1.4kPa ± 0.18kPa when quantified with nonlinear parameters (Fig. 4f). Elasticity maps in the 2D plane capture similar edge effects and a highly heterogeneous internal elasticity distribution shown by the wide-ranging distribution of elasticity values (Fig. 4g). Importantly, the distributions between both linear and nonlinear cases follow similar trends, though the nonlinear case generates a slightly elevated tail of high stiffness. An explanation for the location-specific elasticity properties detected within the lymph node may lie in the structure of the tissue [51, 52]. The murine lymph node is surrounded by a narrow coating of collagen, within which lies an external sinus region of lymphatic endothelial cells for transportation of lymphatic fluid surrounding an internal lymph node stroma. This interior stromal region contains additional, interpenetrating sinus regions that organize a dense mesh of lymphatic vessels used for drainage. The layer of decreased stiffness observed along the exterior of the tissue may correspond to the external sinus region within the node; similarly, the increased stiffness observed in the upper half of the XY plane shown (Fig. 4e) may overlap with the dense region of vasculature used to aid in drainage and the structures observed within the histology images (Supplemental Figure 9). As the anatomy of the lymph node has been mainly characterized by fixed-tissue histology and depth-limited confocal imaging [53], our technique has the potential to improve existing understanding by tracking the elastic properties of the fresh tissue itself.

Thus, we demonstrate μElastography's ability to measure stiffness at the whole organ scale. This spatial map captures the intricacies of the internal structure while preserving the intact 3D geometry. Although some anatomical details may be lost by the smoothing of the registration produced deformation fields – a necessary step to avoid any signal artifacts – the resulting map still quantifies variations in the internal heterogeneities of elastic properties throughout the plane.

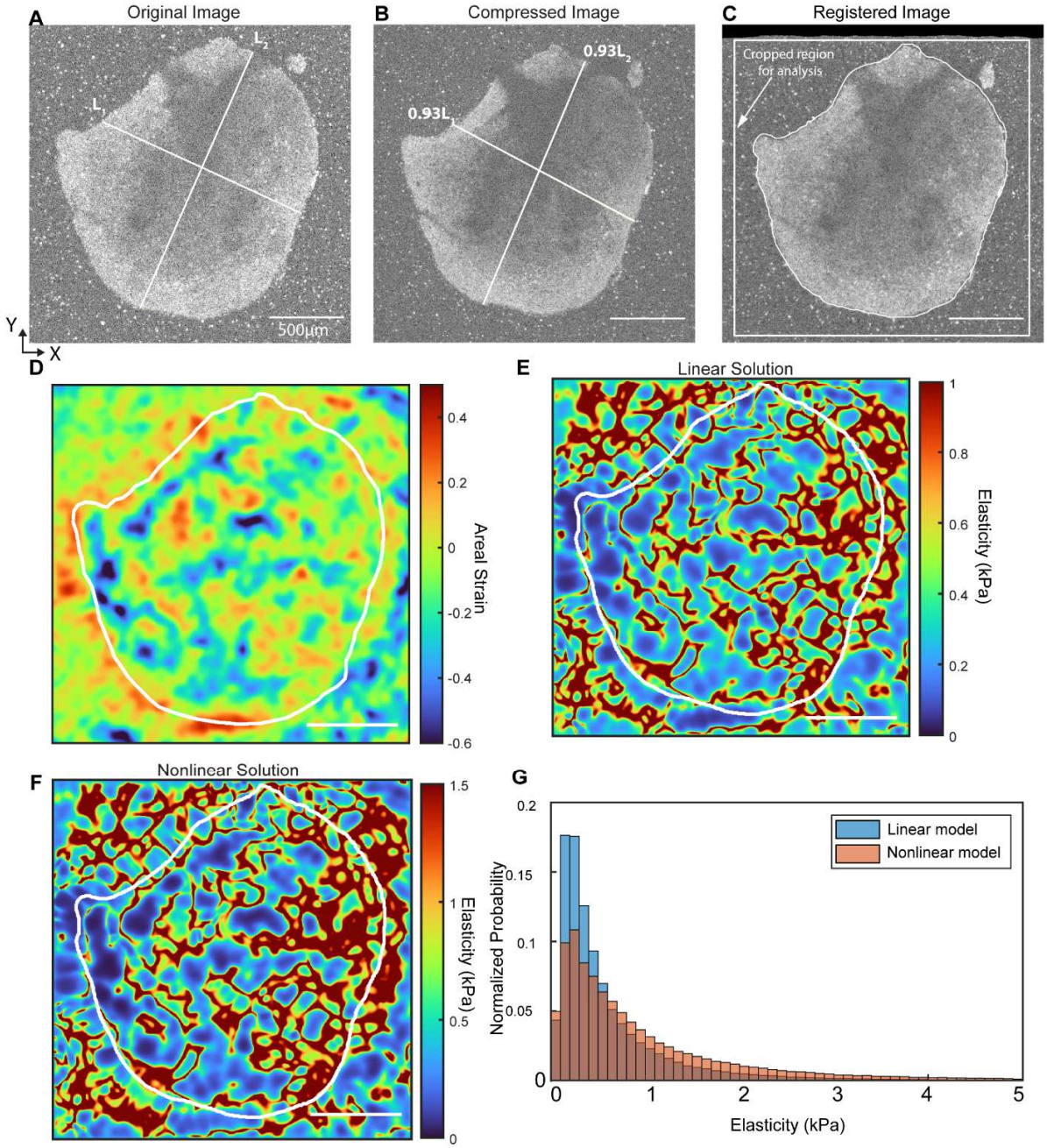

4. Discussion

We have presented here the framework, validation, and application of our μElastography platform. This platform delivers small, multi-directional compressive stresses to embedded biological samples via thermo-responsive hydrogel. By leveraging high resolution optical microscopy coupled with inverse-problem solving algorithms, we derive the internal elastic properties of various biological and biomaterial samples of interest. Existing methods for elastography focus mainly on 2D system perturbations, failing to fully capture the inherent 3D nature of tissues. Furthermore, the majority of existing methods also do

not present elasticity values in absolute units. The combination of 3D compression and imaging, coupled with the use of a reference elasticity gel, addresses the main limitations within current methods in a scalable framework for future studies.

Our platform combines experimental compression (multiaxial stress) with validated computational tools – namely, image registration and inverse problem solving. The application of confined, multi-axial stresses offers a benefit over the uniaxial compressions typically observed in shear wave or strain elastography; in these modalities, variations in stiffness that lie perpendicular to the axis of compression cannot be used for stiffness quantification. In contrast, the multi-axial actuation and imaging performed in our system captures these out of plane heterogeneities. Furthermore, multi-axial compression reduces the number of model assumptions (e.g., uniform stress) necessary to carry out calculations. Image registration [32, 33] has been previously explored in various contexts, including biomedical image stabilization and ultrasound elastography, and more recently in mapping strains in the active lung [54]. Here, we apply this imaging tool to match the relaxed and deformed images to obtain a fully resolved, 3D deformation field with pixel accuracy defined by the optical microscopy mode. From this field, strain fields and stress tensors are calculated using the gradient of the displacement field; in solving the inverse problem, these strains are additionally calculated by relating the Cauchy stress tensor to the deformation field. Importantly, we demonstrate the flexibility of our platform to solve for either linear or nonlinear material properties; the solution's accuracy can be increased when nonlinear properties are known and well-characterized for the biological specimen of interest.

To evaluate the capability of this platform to characterize biomechanical properties of fresh tissues and the intriguing applications it can hold in mechanobiology, we first verify the platform's accuracy using a hydrogel phantom with embedded PA mechanical heterogeneities (Fig. 2). Our phantom components exhibit individual elasticities ranging from ~3 – 30kPa; though high, this range of internal stiffness is biologically relevant when considering diseased tissues can exhibit 4x – 10x increases in stiffness compared to healthy counterparts [4, 5, 7, 55] and individual malignant cells can exhibit 2x – 5x reductions in stiffness compared to healthy cells [56]. As we observe potential nonlinearities in strain response, we apply both nonlinear and linear solvers to the experimental data. Both solvers detect similar values for reference gel, and the nonlinear solver is more adept at detecting the PA inclusions. However, for both solvers, the bulk of the phantom presents as statistically stiffer than its independent AFM measurement; we believe this difference may arise as a result of the internal 3D mechanical structure not quantified by surface AFM measurements, as well as the intrinsic differences in elasticity calculation (i.e., Hertzian curve fitting vs. inverse problem solving).

We then apply the platform to biological samples to generate maps at the cell- and tissue-scales. Within multicellular spheroids (Fig. 3), we detect and characterize the internal stiffness distributions that arise from the complex cell-cell and cell-matrix interactions within a single plane of the bulk of the spheroid. We find highly heterogeneous internal distributions of elasticity that, upon averaging, are comparable to 1kPa AFM measurements of similarly sized spheroids [7, 48] and single cell AFM measurements that have been found to range from 380Pa – 5kPa [48-50]. The high degree of heterogeneity agrees with the heterogeneous local measurements seen in other in vitro stiffness measurements [31]. Recent work in our lab demonstrated how different biological length scales exhibit variations in solid stress: a mechanical stress that arises from the physical forces contained within the solid components of tissue and that is closely related to tissue stiffness [7]. The balancing of internal mechanical properties that we see presented as redistributions of stiffness across X- and Y-directions and between spheroid samples may therefore relate to biophysical mechanisms for enabling cell survival within the specific local environment. An intriguing future application would involve measuring solid stress and stiffness

heterogeneity in tumors simultaneously, to test the hypothesis that stiffness heterogeneity may provide protections for cancer cell against high level of solid stresses [7].

We further apply the platform to intact murine lymph nodes to highlight the 3D capabilities and potentials of the system. We find heterogeneous distributions of stiffness within an interior plane of the tissue, varying between ~0.2 to >2kPa; between tissues, we find an average stiffness ranging between 0.64kPa and 1.4kPa. A recent study of immunologically challenged murine lymph nodes cited a range in whole-tissue Young's modulus from ~0.6kPa to ~1.25kPa, increasing in stiffness after challenge and comparable in scale to the values we calculate here [51]. This increase in stiffness following immunological challenge is tied to the organ's role in immune response and disease progression as immune cells accumulate and sequester. As solid stresses are known to remodel the tissue microenvironment (e.g., compressing blood vessels, remodeling extracellular matrix) and were recently discovered to restrict lymphocyte infiltration into metastatic lymph nodes [57], the distributions of stiffness we observe may play a key role in directing immune cell localization or expansion when the system is challenged. The extension of our technique to include fluorescent immune cells could serve to further elucidate the mechanisms of immune response and lymph node micro/macro metastasis within the lymph node [4]. However, it would be important to choose cell populations with a low or nonexistent motility (e.g., cancer cells and resident cells in the lymph node) to prevent artifacts from cell migration – not sample compression – during the registration process.

The actuations used here produced a nearly isotropic strain field of high magnitude. Focusing on single 2D planes, we quantify the areal strain by considering the stretch in X- and Y-directions. In some cases, these areal strain values exceed 50%, implying isotropic strains along the X- and Y-directions of ~30%; strains of this magnitude would suggest the risk of tissue damage. However, histology of compressed and control lymph nodes (Supplemental Figure 9) indicates this is not the case within the strain regime applied. These observed high magnitude strains may further suggest that a nonlinear elastic model such as a neo-Hookean hyperelastic solid may be more appropriate than the linear models presented here. We first characterize the stress-strain response of reference agarose (0.5% w/v) and find linear behaviors up to strains of 40%, supporting our use of the linear model within this regime (Supplemental Figure 10). Indeed, comparisons between nonlinear and linear elasticity maps for the biological samples studied here show a high degree of agreement between the linear and nonlinear models; nonlinear models are more sensitive to the presence of affine-induced strain artifacts and typically show marginally higher and tighter distributions than the linear counterparts. Based on this comparison of the linear vs nonlinear model and for the ease of simplicity, we suggest the use of the linear formulation of the AWE inverse problem for observed strain values below 40%. We would further encourage measurement of the elasticity map at low strains to ensure the linearity assumption, and to perform the repeated and averaged measurement to improve the signal-to-noise ratio.

There are certain assumptions within our platform that are currently unavoidable, though future optimizations could improve them. Integral to the execution of our elastography method is the assignment of the system's boundary conditions: among these are a boundary Poisson's ratio (PR) as well as a boundary elasticity. Here we choose to use a directly measured Poisson's ratio for agarose of 0.36 while the majority of published Poisson's ratios for agarose are cited at 0.5 (incompressible). A similar discrepancy arises when considering biological tissues. Most biological tissues are assumed as incompressible (PR = 0.5) or nearly incompressible (PR = 0.45), while several other studies have cited PR as low as 0.1 – 0.2 [4, 58, 59] or up to 0.4 [60]. Thus, defining a Poisson's ratio that accurately captures both reference and biological materials is challenging. Our current inverse problem design is limited in its ability to assign multiple Poisson's ratios to interior regions, a limitation which represents a future

improvement in ongoing development of the elastography system. Furthermore, the data and elasticity maps presented here were calculated with a certain degree of smoothing applied to the input deformation fields. This smoothing is necessary to remove the basal noise inherent to registered fields (Supplemental Figure 1) and delineate sample locations, but in turn loses measurement resolution. Indeed, the idea of elasticity resolution has previously been explored in the context of optical coherence elastography, where studies have closely linked elastography resolution with the type and degree of the mechanical deformation [61]. Furthermore, the smoothing of deformation fields must be performed with moderation, as too much smoothing can reduce the signal to such an extent as to artificially elevate the apparent stiffness of the sample. Future improvements to the computational platform would include characterizing the stiffness tensor in 3D to prevent any artifacts from potentially anisotropic stresses that arise during the compression process, and ideally contribute to more resolved spatial elasticity maps.

Though our experiments here demonstrate the utility and robustness of our experimental and computational framework, some challenges exist when optimizing the system for biological applications. At the multicellular scale, optical scattering limits the size of spheroids capable of being measured. Additional technical challenges arise with respect to preparing and actuating the sample complex for multicellular spheroids: in addition to the delicate process of ensuring spheroids are fully embedded within reference gel, the nature of the embedding complex may be prohibitive to most common cell viability assays (e.g., Propidium iodide, MTT), requiring faster timelines for sample preparation and actuation to avoid cell damage. Although whole organs are less susceptible to longer sample preparation and actuation times, technical limitations of imaging depth affect the range of mapping possible. Furthermore, precise embedding of the tissue within the central plane of the reference agarose may be challenging to standardize, making it difficult to co-register elastography maps with histology images.

Because of the challenges cited above, improvements across certain technical aspects will aid future applications of the μElastography platform. Most prominent among these are improvements to imaging resolution and capabilities that will enable additional size-scaling and higher resolution elasticity maps. In the experiments described here, we utilize confocal microscopy (imaging depth 40-50μm) and OCT (imaging depth 2mm); the platform is additionally compatible with multi-photon microscopy (imaging depth of 500μm). These modalities are limited in the field of view and depth of focus they can capture, and a higher depth-penetrating imaging method would enable larger 3D imaging and elasticity mapping. When coupled with recent developments in tissue clearance [62, 63], these imaging improvements will be particularly advantageous in the context of mapping larger intact organ tissue such as the murine brain. Furthermore, accurate registration relies heavily on feature excitation and contrast: when these factors are lacking the image registration software struggles to accurately connect blank spaces between relaxed and deformed conditions, requiring additional smoothing to reduce artificial noise artifacts from the raw registration. Improvements to biocompatible contrast agents to perfuse through animal subjects pre-sacrifice would help to increase depth and resolution of mapping. An additional method can be also implemented as a supplement or replacement to the use of the reference agarose in boundary conditions. The placement of deformable polyacrylamide beads (Supplemental Figure 11) at the surface of tissue would supply a direct, quantitative measurement of applied stress [7] as their deformation and AFM-calculated stiffness are coupled to produce an applied stress map around the sample. Such an addition to the experimental design would be particularly useful in cases where stress application is isotropic or sample boundaries are irregularly shaped.

5. Conclusion

The spatial maps generated by the μElastography platform highlight the distributions of stiffness present at the multicellular scale that remain hidden when using traditional macroscale mechanical

characterizations. With our method, we have combined advantages from existing methods for mechanical characterization (e.g., high resolution imaging, intact/3D tissue samples, and biocompatibility; see Table 1) while attempting to overcome existing disadvantages (e.g., relative values, non-scalability). The final product is a platform compatible with multiple imaging modalities, multiple biological length scales, and multiple mechanical measurements of interest.

Importantly, there is potential for scaling the platform across the extremes of biological length-scales. At the single cell level [64], there has long been interest to map the internal elasticity of cells. The methods to do so, however, typically rely on AFM [65] or only generate local measurements [31, 66]. Our platform offers the potential to measure spatial distributions of elastic properties within single cells using such fiducial markers as fluorescent mitochondria or florescent proteins, building off of previous methods using internally generated traction forces [67]. Within tissues, pathways such as the complex mechanoimmune responses as well as specific behaviors of immune cells could be quantified by incorporating in fluorescent expressing neutrophils or macrophages as they migrate or sequester within tissues. At the whole organ level, entire organs such as the murine brain could be mapped to track age- and disease-related changes in elasticity within the entire organ [68, 69].

The field of mechanobiology has experienced a resurgence of interest in understanding biomechanical properties and mechanical cues, and their effect on health and disease. Our technique bridges the gaps in existing technologies to provide highly detailed, absolute measurements of biological stiffness and promises to deliver elastic information across a range of biological length-scales.

Acknowledgements

H.T.N. acknowledges support from the National Institutes of Health R21EB031332 and DP2HL168562, a Beckman Young Investigator Award, an NSF CAREER Award, Boston University Center for Multiscale and Translational Mechanobiology, and a Dean's Catalyst Award. We thank the Neurophotonics Center at Boston University for their generous support and access to their facility. We are especially grateful to Paul Barbone for sharing the AWE inverse problem code and offering helpful guidance regarding analysis and mechanical models. Histology services were obtained via the Boston University Collaborative Research Laboratory (CoRE). The research reported in this publication was supported in part by the Boston University Micro and Nano Imaging Facility and the Office of the Director, National Institutes of Health of the National Institutes of Health under award Number S10OD024993. The content is solely the responsibility of the authors and does not necessarily represent the official views of the National Institutes of Health.

Author contributions: K.R. and H.T.N. conceived the project and wrote the manuscript. K.R. developed and executed experiments, analyzed data, and wrote the manuscript. R.L. developed image registration pipeline and strain analysis, derived nonlinear AWE formulation, adapted linear AWE formulation, and ran Abacus simulations. J.M. designed and optimized imaging stage. S. Zheng cultured multicellular spheroids and assisted in animal sacrifice. S. Zheng and S. Zhang carried out AFM measurements. S. Zhang ran Abacus simulations. R.B. contributed to data analysis and animal sacrifice. H.T.N. supervised the project and provided guidance on experimental design, data collection, data interpretation, and writing the manuscript.

802 **Table 1:** Various techniques for mechanical characterization of biological tissues

Technique	**Characteristic Sizescale (m)**	**Advantages**	**Disadvantages**	**Reference**
µElastography	10^{-7} – 10^{-3}	Detailed spatial elasticity maps	Depth of mapping limited by microscope capabilities	
		Multi-plane characterization	Low strain sensitivity	
		Precisely control 3D mechanical perturbation		
		Scalable across biological samples & imaging modalities		
		Absolute elasticity values		
Atomic Force Microscopy (AFM)	10^{-9} – 10^{-6}	High resolution elasticity maps	Requires tissue sectioning	[18]
			Limited to 2D Surface mapping	
Microrheology	10^{-9} – 10^{-6}	Capture precise viscoelastic properties	Limited to micron-range local measurements	[20-22]
			Non-compatible for larger biological length scales	
Cell biomechanical imaging	10^{-7} – 10^{-4}	Subcellular spatial resolution	Measurements dependent on internal fiducial markers	[67]
		Accounts for heterogeneous internal modulus	Limited by scale and material assumptions	
		Cell-cell comparisons possible		
Brillouin Microscopy	10^{-7} –10^{-6}	3D mechanical maps	Non-translatable units	[24, 25]
		Subcellular resolution		
Tensile testing	10^{-3} – 10^{-1}	High throughput testing	Bulk properties only; no spatial information	[70, 71]
		Precise control of 2D strain	Destructive to tissue	
Compression / Shear testing	10^{-3} – 10^{-1}	High throughput testing	Bulk properties only; no spatial information	[72]
		Precise control of 2D strain	2D strain only	
Magnetic Resonance elastography	10^{-4} – 10^{-3}	Highly biocompatible & noninvasive	Inability to decouple tissue modulus from tissue density	[73, 74]
			Low spatial resolution incompatible with cellular level mapping	

			Imaging size decreases at higher resolution	
Ultrasound elastography	10^{-4}	Highly biocompatible & noninvasive	Inability to decouple tissue modulus from tissue density	[75]
			Low spatial resolution incompatible with cellular level mapping	
		Compatible with strain or shear wave perturbations	Tissue can attenuate signal	
Optical Coherence elastography	10^{-5} – 10^{-4}	Sensitive to small mechanical changes	Inability to decouple tissue modulus from tissue density	[23, 28, 76]
		Highly biocompatible	Limited penetration depth	
Microtweezers	10^{-5}	Precisely controlled 2D stresses	Limited to strain measurements	[26, 27]
			Limited scalability	
Deformable oil droplets	10^{-5}	Enables tracking temporal evolution of properties	Local measurements only	[30]
		Precisely controlled 3D stress	Limited Scalability	
Thermo-responsive sensors	10^{-5}-10^{-4}	Temporal evolution of mechanical properties	Local measurements only	[31]
			Limited scalability	
			Limited comparison to existing methods	
Computational Neural Networks	10^{-7}-10^{-2}	Incorporates non-homogeneous material properties	Limited to 2D plane perturbation	[44]
Laser Speckle Rheology	10^{-5}	Noninvasive	Limited comparison to existing methods	[29]
		High spatial resolution		

Table 2: Youngs modulus of component hydrogel by sample | Measurements taken by AFM and quantified via appropriate Hertz model for sphere-on-sphere contact or sphere-on-surface contact.

Sample of interest	**Component**	**Fluorescent Tracers**	**Young's Modulus ± SE**
Validation Phantom: AFM	PA Inclusions	Red, 1-5µm	29.3 ± 2.3 kPa
	Phantom Agarose	Red, 1-5µm	2.67 ± 0.10 kPa
	Reference Hydrogel	Green, 1-5µm	7.83 ± 0.25 kPa
Validation Phantom: uElastography, Linear	PA inclusions	Red, 1-5µm	16.7 ± 1.92kPa
	Phantom Agarose	Red, 1-5µm	6.1 ± 0.24kPa
	Reference	Green, 1-5µm	7.6 ± 0.32kPa

	Hydrogel		
Validation Phantom: uElastography, Nonlinear	PA inclusions	Red, 1-5µm	32.17 ± 5.08kPa
	Phantom Agarose	Red, 1-5µm	5.97 ± 0.37kPa
	Reference Hydrogel	Green, 1-5µm	8.41 ± 0.65kPa

Disclosures

The authors have no competing interests to disclose.

Reference

[1] A.J. Engler, S. Sen, H.L. Sweeney, D.E. Discher, Matrix Elasticity Directs Stem Cell Lineage Specification, Cell 126(4) (2006) 677-689.

[2] D.E. Discher, P. Janmey, Y.-L. Wang, Tissue Cells Feel and Respond to the Stiffness of Their Substrate, Science 310(5751) (2005) 1139-1143.

[3] H.T. Nia, L.L. Munn, R.K. Jain, Physical traits of cancer, Science (New York, N.Y.) 370(6516) (2020).

[4] H.T. Nia, H. Liu, G. Seano, M. Datta, D. Jones, N. Rahbari, J. Incio, V.P. Chauhan, K. Jung, J.D. Martin, V. Askoxylakis, T.P. Padera, D. Fukumura, Y. Boucher, F.J. Hornicek, A.J. Grodzinsky, J.W. Baish, L.L. Munn, R.K. Jain, Solid stress and elastic energy as measures of tumour mechanopathology, Nature Biomedical Engineering 1 (2016).

[5] G. Seano, H.T. Nia, K.E. Emblem, M. Datta, J. Ren, S. Krishnan, J. Kloepper, M.C. Pinho, W.W. Ho, M. Ghosh, V. Askoxylakis, G.B. Ferraro, L. Riedemann, E.R. Gerstner, T.T. Batchelor, P.Y. Wen, N.U. Lin, A.J. Grodzinsky, D. Fukumura, P. Huang, J.W. Baish, T.P. Padera, L.L. Munn, R.K. Jain, Solid stress in brain tumours causes neuronal loss and neurological dysfunction and can be reversed by lithium, Nature Biomedical Engineering 3(3) (2019) 230-245.

[6] H.T. Nia, M. Datta, G. Seano, P. Huang, L.L. Munn, R.K. Jain, Quantifying solid stress and elastic energy from excised or in situ tumors, Nat Protoc 13(5) (2018) 1091-1105.

[7] S. Zhang, G.N. Grifno, R. Passaro, K. Regan, S. Zheng, M. Hadzipasic, R. Banerji, L. O'Connor, V. Chu, S.Y. Kim, J. Yang, L. Shi, K. Karrobi, D. Roblyer, M.W. Grinstaff, H.T. Nia, Intravital measurements of solid stresses in tumours reveal length-scale and microenvironmentally dependent force transmission, Nature Biomedical Engineering (2023).

[8] T. Stylianopoulos, J.D. Martin, V.P. Chauhan, S.R. Jain, B. Diop-Frimpong, N. Bardeesy, B.L. Smith, C.R. Ferrone, F.J. Hornicek, Y. Boucher, L.L. Munn, R.K. Jain, Causes, consequences, and remedies for growth-induced solid stress in murine and human tumors, Proceedings of the National Academy of Sciences of the United States of America 109(38) (2012) 15101-15108.

[9] M.J. Paszek, N. Zahir, K.R. Johnson, J.N. Lakins, G.I. Rozenberg, A. Gefen, C.A. Reinhart-King, S.S. Margulies, M. Dembo, D. Boettiger, D.A. Hammer, V.M. Weaver, Tensional homeostasis and the malignant phenotype, Cancer Cell 8(3) (2005) 241-254.

[10] F. Bordeleau, B.N. Mason, E. Macklin Lollis, M. Mazzola, M.R. Zanotelli, S. Somasegar, J.P. Califano, C. Maontague, D.J. LaValley, J. Huynh, N. Mencia-Trinchant, Y.L. Negron Abril, D.C. Hassane, L.J. Bonassar, J.T. Butcher, R.S. Weiss, C.A. Reinhart-King, Matrix stiffening promotes a tumor vasculature phenotype, Applied Physical Sciences 114(3) (2016) 492-497.

[11] G. Charras, E. Sahai, Physical influences of the extracellular environment on cell migration, Nature Reviews Molecular Cell Biology 15 (2014) 813-824.
[12] S. Zhang, K. Regan, J. Najera, M.W. Grinstaff, M. Datta, H.T. Nia, The peritumor microenvironment: physics and immunity, Trends in Cancer 9(8) (2023) 609-623.
[13] D.L. Cochlin, R.H. Ganatra, D.F.R. Griffiths, Elastography in the detection of prostatic cancer, Clinical Radiology 57(11) (2002) 1014-1020.
[14] N.F. Boyd, Q. Li, O. Melnichouk, E. Huszti, L.J. Martin, A. Gunasekara, G. Mawdsley, M.J. Yaffe, S. Minkin, Evidence that breast tissue stiffness is associated with risk of breast cancer, PloS One 9(7) (2014).
[15] A. Stylianou, F. Mpekris, C. Voutouri, A. Papoui, A. Constantinidou, E. Kitiris, M. Kailides, T. Stylianopoulos, Nanomechanical properties of solid tumors as treatment monitoring biomarkers, Acta Biomaterialia 154 (2022) 324-334.
[16] C. Voutouri, F. Mpekris, M. Panagi, C. Krolak, C. Michael, J.D. Martin, M.A. Averkiou, T. Stylianopoulos, Ultrasound stiffness and perfusion markers correlate with tumor volume responses to immunotherapy, Acta Biomaterialia (In press) (2023).
[17] A. Stylianou, C. Voutouri, F. Mpekris, T. Stylianopoulos, Pancreatic cancer presents distinct nanomechanical properties during progression, Ann Biomed Eng 51 (2023) 1602-1615.
[18] M. Krieg, G. Fläschner, D. Alsteens, B.M. Gaub, W.H. Roos, G.J.L. Wuite, H.E. Gaub, C. Gerber, Y.F. Dufrêne, D.J. Müller, Atomic force microscopy-based mechanobiology, Nature Reviews Physics 1 (2018) 41-57.
[19] B. Han, H.T. Nia, C. Wang, P. Chandrasekaran, Q. Li, D.R. Chery, H. Li, A.J. Grodzinsky, L. Han, AFM-Nanomechanical Test: An interdisciplinary tool that links the understanding of cartilage and meniscus biomechanics, osteoarthritis degeneration, and tissue engineering, ACS Biomaterials Science & Engineering 3(9) (2017) 2033-2049.
[20] Y. Tseng, T.P. Kole, D. Wirtz, Micromechanical mapping of live cells by multiple-particle-tracking microrheology, Biophysical Journal 83(6) (2002) 3162-3176.
[21] S.N. Ricketts, J.L. Ross, R.M. Robertson-Anderson, Co-entangled actin-microtubule composites exhibit tunable stiffness and power-law stress relaxation, Biophysical Journal 115(6) (2018).
[22] R.M. Robertson-Anderson, Optical tweezers microrheology: from the basics to advanced techniques and applications, ACS Macro Letters 7(8) (2018) 968-975.
[23] B.F. Kennedy, P. Wijesinghe, D.D. Sampson, The emergence of optical elastography in biomedicine, Nature Photonics 11 (2017) 215-221.
[24] G. Scarcelli, W.J. Polacheck, H.T. Nia, K. Patel, A.J. Grodzinsky, R.D. Kamm, S.H. Yun, Noncontact three-dimensional mapping of intracellular hydromechanical properties by Brillouin microscopy, Nature Methods 12 (2015) 1132-1134.
[25] J. Zhang, M. Nikolic, K. Tanner, G. Scarcelli, Rapic biomechanical imaging at low irradiation level via dual line-scanning Brillouin microscopy, Nature Methods (2023).
[26] D. Jaiswal, N. Cowley, Z. Bian, G. Zheng, K.P. Claffey, K. Hoshino, Stiffness analysis of 3D spheroids using microtweezers, Plos One 12(11) (2017).
[27] D. Jaiswal, Z. Moscato, Y. Tomizawa, K.P. Claffey, K. Hoshino, Elastography of multicellular spheroids using 3D light microscopy, Biomedical Optics Express 10(5) (2019).
[28] Y. Lin, N. Leartprapun, J.C. Luo, S.G. Adie, Light-sheet photonic force optical coherence elastography for high-throughput quantitative 3D micromechanical imaging, Nature Communications 13(1) (2022).
[29] Z. Hajjarian, H.T. Nia, S. Ahn, A.J. Grodzinsky, R.K. Jain, S.K. Nadkarni, Laser speckle rheology for evaluating the viscoelastic properties of hydrogel scaffolds, Scientific Reports 6 (2016).

[30] F. Serwane, A. Mongera, P. Rowghanian, D.A. Kealhofer, A.A. Lucio, Z.M. Hockenbery, O. Campàs, *In vivo* quantification of spatially varying mechanical properties in developing tissues, Nature Methods 14 (2017) 181-186.
[31] S. Mok, S. Al Habyan, C. Ledoux, W. Lee, K.N. MacDonald, L. McCaffrey, C. Moraes, Mapping cellular-scale internal mechanics in 3D tissues with thermally responsive hydrogel probes, Nat Commun 11(1) (2020) 4757.
[32] M.P. Heinrich, O. Maier, H. Handels, Multi-modal multi-atlas segmentation using discrete optimisation and self-similarities, Visceral Challenge@ ISBI 1390 (2015).
[33] M.P. Heinrich, M. Jenkinson, M. Brady, J.A. Schnabel, MRF-based deformable registration and ventilation estimation of lung CT, IEEE Translational Medical Imaging 32 (2013) 1239-1248.
[34] P.E. Barbone, Adjoint-weighted variational formulation for the direct solution of plane stress inverse elasticity problems, Jounrnal of Physics: Conference Series 135 (2008).
[35] P.E. Barbone, C.E. Rivas, I. Harari, U. Albocher, A.A. Oberai, Y. Zhang, Adjoint-weighted variational formulation for the direct solution of inverse problems of general linear elasticity with full interior data, International Journal for Numerical Methods in Engineering (2010).
[36] A.M. Akimoto, E. Hasuike, H. Tada, K. Nagase, T. Okano, H. Kanazawa, R. Yoshida, Design of Tetra-arm PEG-crosslinked Thermoresponsive Hydrogel for 3D Cell Culture, Analytical Sciences 32 (2016) 1203-1205.
[37] A.M. Akimoto, E.H. Niitsu, K. Nagase, T. Okano, H. Kanazawa, R. Yoshida, Mesenchylmal Stem Cell Culture on Poly(N-isopropylacrylamide) Hydrogel with Repeated Thermo-Stimulation, Int J Mol Sci 19(4) (2018).
[38] W. Lee, N. Kalashnikov, S. Mok, R.K. Halaoui, E. , A.J. Putnam, S. Takayama, M. Park, L. McCaffrey, R. Zhao, R.L. Leask, C. Moraes, Dispersible hydrogel force sensors reveal patterns of solid mechanical stress in multicellular spheroid cultures, Nature Communications 10 (2019).
[39] J.L. Hutter, J. Bechhoefer, Calibration of atomic-force microscope tips, Review of Scientific Instruments 64 (1993) 1868-1873.
[40] M. Salerno, S. Dante, N. Patra, A. Diaspro, AFM measurement of the stiffness of layers of agarose gel patterned with polylysine, Microscopy Research & Technique (73) (2010) 982-990.
[41] G. Bertalan, P. Boehm-Sturm, S. Schreyer, A.-S. Morr, B. Steiner, H. Tzschätzsch, J. Braun, J. Guo, I. Sack, The influence of body temperature on tissue stiffness, blood perfusion, and water diffusion in the mouse brain, Acta Biomaterilia 96 (2019) 412-420.
[42] M. Plodinec, M. Loparic, C.A. Monnier, E.C. Obermann, R. Zanetti-Dallenbach, P. Oertle, J.T. Hyotyla, U. UAebi, M. Bentires-Alj, R.Y.H. Lim, C. Schoenenberger, The nanomechanical signature of breast cancer, Nature Nanotechnology 7 (2012) 757-765.
[43] C.M. McCarthy, J.M. Allardyce, S.E. Hickey, M.T. Walsh, K.D. McGourty, J.J.E. Mulvihill, Comparison of macroscale and microscale mechanical properties of fresh and fixed-frozen porcine colonic tissue, Journal of the Mechanical Behavior of Biomedical Materials 138 (2023).
[44] A. Kamali, M. Sarabian, K. Laksari, Elasticity imaging using physics-informed neural networks: Spatial discovery of elastic modulus and Poisson's ratio, Acta Biomaterialia 155 (2023) 400-409.
[45] H.T. Nia, L. Han, Y. Li, C. Ortiz, A.J. Grodzinsky, Poroelasticity of cartilage at the nanoscale, Biophysical Journal 101(9) (2011) 2304-2313.
[46] G. Bertalan, J. Becker, H. Tzschätzsch, A. Morr, H. Herthum, M. Shahryari, R.D. Greenhalgh, J. Guo, L. Schröder, C. Alzheimer, S. Budday, K. Franze, J. Braun, I. Sack, Mechanical behavior of the hippocampus and corpus callosum: An attempt to reconcile

ex vivo with in vivo and micro with macro properties, Journal of the Mechanical Behavior of Biomedical Materials 138 (2023).
[47] S. Abuhattum, P. Kotzbeck, R. Schlüßler, A. Harger, A.A. de Schellenberger, K. Kim, J.-C. Escolano, T. Müller, J. Braun, M. Wabitsch, M. Tschöp, I. Sack, M. Brankatschk, J. Guck, K. Stemmer, A.V. Taubenberger, Adipose cells and tissues soften with lipid accumulation while in diabetes adipose tissue stiffens, Scientific Reports 12 (2022).
[48] M. Hadzipasic, S. Zhang, Z. Huang, R. Passaro, M.S. Sten, G.M. Shankar, H.T. Nia, Emergence of nanoscale viscoelasticity from single cancer cells to established tumors, (In Review).
[49] K. Wang, Y. Qin, Y. Chen, In situ AFM detection of the stiffness of the in situ exposed cell nucleus, Biochimica et Biophysica Acta - Molecular Cell Research 1868(5) (2021).
[50] A.B. Mathur, A.M. Collinsworth, W.M. Reichert, W.E. Kraus, G.A. Truskey, Endothelial, cardiac muscle and skeletal muscle exhibit different viscous and elastic properties as determined by atomic force microscopy, Journal of Biomechanics 34 (2001) 1545-1553.
[51] F.P. Assen, J. Abe, M. Hons, R. Hauschild, S. Shamipour, W.A. Kaufmann, T. Costanzo, G. Krens, M. Brown, B. Ludewig, S. Hippenmeyer, C.-P. Heisenberg, W. Weninger, E. Hannezo, S.A. Luther, J.V. Stein, M. Sixt, Multitier mechanics control stromal adaptations in the swelling lymph node, Nature Immunology 23 (2022) 1246-1255.
[52] S. Jalkanen, M. Salmi, Lymphatic endothelial cells of the lymph node, Nature Reviews Immunology 20 (2020) 566-578.
[53] I.L. Grigorova, M. Panteleev, J.G. Cyster, Lymph node cortical sinus organization and relationship to lymphocyte egress dynamics and antigen exposure, Proceedings of the National Academy of Sciences 107 (2010) 20447-20452.
[54] R. Banerji, G.N. Grifno, L. Shi, D. Smolen, R. LeBourdais, J. Muhvich, C. Eberman, B. Hiller, J. Lee, K. Regan, S. Zheng, S.S. Zhang, J. Jiang, J.C. Breda, R. Pihl, K. Traber, S. Mazzilli, G. Ligresti, J.P. Mizgerd, B. Suki, H.T. Nia, Crystal ribcage: a platform for probing real-time lung function at cellular resolution in health and disease, Nature Methods (2023).
[55] R.G. Wells, Tissue mechanics and fibrosis, Biochimica et Biophysica Acta 1832(7) (2013) 884-890.
[56] W. Xu, R. Mezencev, K. B., L. Wang, J. McDonald, T. Sulchek, Cell Stiffness is a Biomarker of the Metastatic Potential of Ovarian Cancer Cells, PloS ONE 7(10) (2012).
[57] D. Jones, Z. Wang, I.X. Chen, S. Zhang, R. Banerji, P.J. Lei, H. Zhou, V. Xiao, C. Kwong, J.W.M. van Wijnbergen, E.R. Pereira, B.J. Vakoc, P. Huang, H.T. Nia, T.P. Padera, Solid stress impairs lymphocyte infiltration into lymph-node metastases, Nature Biomedical Engineering 2021 5:12 5(12) (2021) 1426-1436.
[58] T. Stylianopoulos, J.D. Martin, M. Snuderl, F. Mpekris, S.R. Jain, R.K. Jain, Coevolution of solid stress and interstitial fluid pressure in tumors during progression: implications for vascular collapse, Cancer Res 73(13) (2013) 3833-41.
[59] J.S. Jurvelin, M.D. Buschmann, E.B. Hunziker, Optical and mechanical determination of poisson's ratio of adult bovine humeral articular cartilage, Journal of Biomechanics 30(3) (1997) 235-241.
[60] D.C. Stewart, A. Rubiano, K. Dyson, C.S. Simmons, Mechanical characterization of human brain tumors from patients and comparison to potential surgical phantoms, PloS One 12(6) (2017) e0177561.
[61] M.S. Hepburn, P. Wijesinghe, L. Chin, B.F. Kennedy, Analysis of spatial resolution in phase-sensitive compression optical coherence elastography, Biomedical Optics Express 10 (2019).

[62] M. Stefaniuk, E.J. Gualda, M. Pawlowska, D. Legutko, P. Matryba, P. Koza, W. Konopka, D. Owczarek, M. Wawrzyniak, P. Loza-Alvarez, L. Kaczmarek, Light-sheet microscopy imaging of a whole cleared rat brain with Thy1-GFP transgene, Scientific Reports 6 (2016).
[63] I. Costantini, J.-P. Ghobril, A.P. DiGiovanna, A.L.A. Mascaro, L. Silvestri, M.C. Müllenbroich, L. Onofri, V. Conti, F. Vanzi, L. Sacconi, R. Guerrini, H. Markram, G. Iannello, F.S. Pavone, A versatile clearing agent for multi-modal brain imaging, Scientific Reports 5 (2015).
[64] A. Touhami, B. Nysten, Y.F. Dufrêne, Nanoscale mapping of the elasticity of microbial cells by atomic force microscopy, Langmuir 19(11) (2003) 4539-4543.
[65] A. Viljoen, M. Mathelié-Guinlet, A. Ray, N. Strohmeyer, Y.J. Oh, P. Hinterdorfer, D.J. Müller, D. Alsteens, Y.F. Dufrêne, Force spectroscopy of single cells using atomic force microscopy, Nature Reviews Methods Primers 1 (2021).
[66] I. Grexa, T. Fekete, J. Molnár, K. Molnár, G. Vizsnyiczai, P. Ormos, L. Kelemen, Single-cell elasticity measurement with an optically actuated microrobot, Micromachines (Basel) 11(9) (2020) 882.
[67] E.P. Canović, D.T. Seidl, S.R. Polio, A.A. Oberai, P.E. Barbone, D. Stamenović, M.L. Smith, Biomechanical imaging of cell stiffness and prestress with subcellular resolution, Biomechanical Modeling in Mechanobiology 13 (2013) 665:678.
[68] T. Takamura, U. Motosugi, Y. Sasaki, T. Kakegawa, K. Sato, K.J. Glaser, R.L. Ehman, H. Onishi, Influence of age on global and regional brain stiffness in young and middle-aged adults, Journal of Magnetic Resonance Imaging 51(3) (2019) 727-733.
[69] M.C. Murphy, J. Huston 3rd, C.R. Jack Jr., K.J. Glaser, A. Manduca, J.P. Felmlee, R.L. Ehman, Decreased brain stiffness in Alzheimer's disease determined by magnetic resonance elastography, Journal of Magnetic Resonance Imaging 34(3) (2011) 494-498.
[70] C.T. McKee, J.A. Last, P. Russell, C.J. Murphy, Indentation versus tensile measurements of Young's modulus for soft biological tissues, Tissue Engineering Part B: Reviews 17 (2011).
[71] L. Rosalia, A. Hallou, L. Cochrane, T. Savin, A magnetically actuated, optically sensed tensile testing method for mechanical characterization of soft biological tissues. , Science Advances 9(2) (2023).
[72] A.S.G. van Oosten, M. Vahabi, A.J. Licup, A. Sharma, P.A. Galie, F.C. MacKintosh, P.A. Janmey, Uncoupling shear and uniaxial elastic moduli of semiflexible biopolymer networks: compression-softening and stretch stiffening, Scientific Reports 6 (2016) 19270.
[73] Y.K. Mariappan, K.J. Glaser, R.L. Ehman, Magnetic Resonance Elastography: A Review, Clinical Anatomy 23(5) (2010) 497-511.
[74] H. Li, G. Flé , M. Bhatt, Z. Qu, S. Ghazavi, L. Yazdani, G. Bosio, I. Rafati, G. Cloutier, Viscoelasticity imaging of biological tissues and single cells using shear wave propagation, Frontiers in Physics 9 (2021).
[75] R.M.S. Sigrist, J. Liau, A.E. Kaffas, M.C. Chammas, J.K. Willmann, Ultrasound elastography: review of techniques and clinical applications, Theranostics 7(5) (2017) 1303-1329.
[76] K.V. Larin, D.D. Sampson, Optical coherence elastography - OCT at work in tissue biomechanics [Invited], Biomed Opt Express 8(2) (2017) 1172-1202.

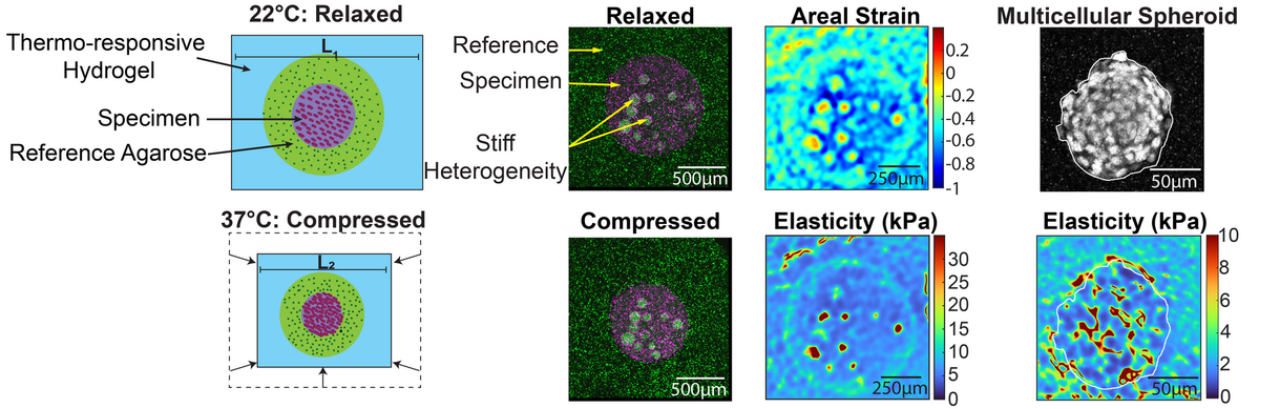
22°C: Relaxed
Thermo-responsive Hydrogel
L1
Specimen
Reference Agarose
37°C: Compressed
L2
Relaxed
Reference
Specimen
Stiff Heterogeneity
500μm
Areal Strain
0.2
0
-0.2
-0.4
-0.6
-0.8
-1
250μm
Multicellular Spheroid
50μm
Compressed
500μm
Elasticity (kPa)
30
25
20
15
10
5
0
250μm
Elasticity (kPa)
10
8
6
4
2
0
50μm